Effect of post-fire lime-saturated water and water–CO_2 cyclic curing on strength recovery of thermally damaged high-performance concrete with different silica contents

Ye Li[a], Haodong Wang[a], Caijun Shi[b], Dujian Zou[a], Ao Zhou[a], Tiejun liu[a,] *

[a] School of Civil and Environmental Engineering, Harbin Institute of Technology, Shenzhen 518055, PR China

[b] College of Civil Engineering, Hunan University, Changsha 410082, China

* Corresponding author. Tel.: +86-0755-26033368

Email adresses : liye@hit.edu.cn (Ye Li), 15818602282@163.com (Haodong Wang), cshi@hnu.edu.cn (Caijun Shi), zoudujian@163.com (Dujian Zou), zhouao@hit.edu.cn (Ao Zhou), liutiejun@hit.edu.cn (Tiejun Liu)

Abstract

This study investigates the effects of lime-saturated water and water–CO_2 cyclic recuring on strength recovery of thermally damaged high-performance concretes (HPC). The HPC samples were subjected to elevated temperatures up to 1000 °C in 200 °C increments and underwent recuring. Phase assemblage and distribution, microstructure evolution, and pore structure of the HPC samples were identified. According to the results, recovered compressive strength of the HPC samples with low silica content can surpass their original strength after 600 and 800 °C exposure and recuring. In contrast, HPC with high silica content is unfavorable for strength recovery at temperatures above 800 °C because the low-calcium phases formed have low reactivity. After 1000 °C exposure, only water–CO_2 cyclic recuring coalesces the disintegrated microstructure and recovers the compressive strength. Strength recovery primarily depends on healing the microcracks and large pores rather than the coarsened cement paste.

Keywords: High-performance concrete, Post-fire curing (recuring), Carbonation, Physicochemical changes, Silica fume content

1. Introduction

Although concrete is noncombustible, fire is detrimental to reinforced concrete (RC) structures due to the drastic degradation of the mechanical properties of concrete at elevated temperatures. Thermal damage to concrete involves a series of physicochemical changes, leading to the coarsening of the microstructure and the creation of contact-type defects [1, 2]. The traditional rehabilitation of fire-damaged RC structures is complex and primarily relies on the removal of damaged concrete and the replacement of patching materials, which is labor-intensive and costly [3, 4]. Therefore, the idea of autogenous self-healing methods such as recuring has been proposed as a novel approach to recovering the performance of fire-damaged concrete [5-13].

During heat exposure, concrete experiences the collapse of calcium–silicate–hydrate (C–S–H), the decomposition of portlandite (at around 480 °C), the change of quartz sand from the α- to β-phase (at 573 °C), and the decarbonation of $CaCO_3$ (between 700 and 800 °C) [5, 14]. Thus, a series of physicochemical changes gives rise to thermal damage to concrete. A few published works on the change of concrete microstructure during recuring demonstrate that the recovery of the mechanical properties of fire-damaged concrete is attributed to the filling of the coarsened pore structure and healing of contact-type defects (microcracks) by the rehydration products [6, 7, 13, 14]. Therefore, the ability of strength recovery of concrete strongly correlates with the degree of thermal damage, the reactivity of the dehydrated products, and the appropriate recuring regimes [6, 8, 15-17].

Poon et al. [7] found that high-strength concrete containing fly ash (FA) offered the best recovery of compressive strength, followed by concrete specimens containing ground granulated blast furnace slag

(GGBFS), condensed silica fume (SF), and metakaolin (MK). This was attributed to the C–S–H produced from the reaction of the $Ca(OH)_2$ with the unhydrated fly ash particles. On the contrary, Akca and Özyurt [11] reported that the concrete with added GGBFS showed a slightly higher strength recovery than that containing pulverized fly ash. The contradiction between these two studies may have originated from the significant difference in their respective mix proportions and the heating method. Unfortunately, there was a lack of microstructural investigation to provide a reasonable explanation. Yim et al. [14] investigated the physicochemical characteristics of thermally damaged normal-strength concrete (NSC) with a water-to-cement ratio (W/C) of 0.5. The decomposition of calcium hydroxide ($Ca(OH)_2$) and calcium carbonate ($CaCO_3$) generated calcium oxide (CaO), the decomposition of C–S–H formed new dicalcium silicate (C_2S), and part of the unhydrated tricalcium silicate (C_3S) maintained. Upon recurring, the rehydration of CaO and C_3S and the carbonation of $Ca(OH)_2$ and CaO occurred, leading to the formation of $Ca(OH)_2$, $CaCO_3$, and C–S–H phases. Apparently, the phase composition of concrete after exposure to heat, affected by the original state of the hydrated system, determines the performance of recuring. A large residue of C_3S and C_2S is beneficial for regaining strength during recuring.

The recuring regime is another decisive factor in strength recovery, and high relative humidity (RH) is necessary for the rehydration of the dehydrated products and the recovery of the mechanical properties of thermally damaged concrete [13, 14]. Lin et al. [6] found that CaO and unhydrated cement grains were rehydrated by absorbing moisture from the surrounding medium, which agrees with the findings of Park et al. [12], demonstrating that sufficient moisture should be supplied to maintain the outer layer of concrete samples in a permanently wet state. Moreover, the inner part of a thermally damaged specimen can be rehydrated if only moisture can penetrate deeply.

The prerequisites for an improved recuring effect mentioned above aroused interest in investigating the related potential of HPC in recuring because of its large fraction of unhydrated cement particles and dense

microstructure [4, 18-20]. In addition, the synthetic fibers included in HPC to increase its ductility and prevent explosive spalling at elevated temperatures can create interconnected microcrack networks after heating, promoting the infiltration of moisture [21, 22]. On the other hand, silica fume or other supplementary cementitious materials (SCMs) are usually added to HPC to facilitate pozzolanic reactions. A decreased calcium-to-silicon ratio (Ca/Si) leads to the formation of low-lime calcium silicates such as dicalcium silicate polymorphs (γ-C_2S), tricalcium disilicate (C_3S_2), and monocalcium silicate (CS) after concrete exposure to heat [23, 24], which are unfavorable for rehydration due to their low hydration reactivity. However, in the presence of moisture and CO_2, these phases exhibit enhanced carbonate reactivity to form calcium carbonates and polymerized silica gel (see Eq. (1)) [25-27], which will be beneficial for healing the thermally damaged microstructure of concrete. Therefore, in addition to curing the thermally damaged concrete in lime-saturated water, carbonation is a promising method for the effective strength recovery of HPC.

$$Ca_xSi_yO_{(x+2y)} + xH^+ + xHCO_3^- \rightarrow ySiO_2 \downarrow + xCaCO_3 \downarrow + xH_2O \quad (1)$$

The abovementioned issues form the motivations for investigating the impact of recuring on the strength recovery of thermally damaged HPC herein. The inclusion of silica fume was selected as a critical factor due to its influence on the chemical composition of hydration products. The concrete samples were exposed to a temperature of 200, 400, 600, 800, and 1000 °C and subsequently recured through two recuring regimes: lime-saturated water and water–CO_2 cyclic conditions. The compressive strength of the concrete samples was analyzed after exposure to heat and recuring. X-ray diffraction (XRD), thermogravimetric analysis (TGA), backscattered electron (BSE) imaging, mercury intrusion porosimetry (MIP), and scanning electron microscopy (SEM) coupled with energy-dispersive X-ray spectrometry (EDX) thoroughly characterized the phase assemblage, microstructure, and porosity of the concrete

samples during rehydration and carbonation to examine the nature of the healing process and reveal the mechanisms for the strength recovery of HPC.

2. Materials and methodology

2.1. Materials and sample preparation

As presented in Table 1, this work investigated three HPC mixtures comprising cement, fine aggregate, silica flour, silica fume, superplasticizer, and water. Considering the water content of superplasticizers, cement was substituted with 0% to 40% silica fume with low water-to-binder ratios between 0.19 to 0.21 to achieve dense microstructures. CEM I 52.5 N Portland cement, standard quartz sand with a maximum grain size of 1.18 mm, silica flour with a median particle size of 125 μm, and LY-0850 silica fume with high pozzolanic activity were used as the raw materials. Table 2 lists the chemical composition of the cement and silica fume. A polycarboxylate-based superplasticizer with a solid content of 24% was also used to obtain proper consistency and workability, and monofilament cylindrical polypropylene (PP) fibers with a length of 12 mm and a diameter of 31 μm were included in the HPC specimens to prevent explosive spalling during heating.

Table 1. The mix proportions of the HPC samples (unit: kg/m^3).

Mix Design	Cement	Fine aggregates	Silica flour	Silica fume	Superplasticizer	Water	Total water	Polypropylene fibers
0SF	969.7	911.5	300.6	0	43.6	174.5	207.6	3
0.2SF	888.2	834.9	275.3	177.6	32.0	191.8	216.1	3
0.4SF	815.2	766.3	252.7	326.1	34.2	205.4	231.4	3

A 15 L planetary mixer prepared the HPC mixtures. The binders (cement and silica fume) and the fillers (silica flour and sieved river sand) were dry-mixed for 3 min to ensure good dispersion. Afterward, 80% of the premixed water and the superplasticizer were gradually added to the dry ingredients and mixed for another 3 min until the fresh mixture was homogenous and consistent. The PP fibers were then dispersed

into the fresh mixture and mixed for another 2 min to achieve good dispersion. Finally, the 20% remaining water was added to the mixture. The HPC mixtures were cast into 50 × 50 × 50 mm^3 cubic molds for the compressive tests, scanning electron microscopy, energy-dispersive X-ray spectrometry, and mercury intrusion porosimetry. In addition, cement pastes without the inclusion of quartz sand and silica flour were prepared for X-ray diffraction and thermogravimetric analysis since quartz has a high diffraction intensity, overshadowing the peaks of the hydration products. Twenty-four hours after casting, the samples were demolded and cured in lime-saturated water for another 27 days before testing.

Table 2. The chemical composition of the cement and silica fume.

	CaO	SiO_2	Al_2O_3	Fe_2O_3	MgO	K_2O	TiO_2	SO_3	SrO
Cement (%)	67.10	19.11	3.84	3.36	1.49	0.84	0.32	3.46	0.25
Silica fume (%)	0.14	96.97	-	0.08	0.35	0.36	-	1.77	-

2.2. Heating and recuring regimes

At a curing period of 28 days, the specimens were subjected to a temperature of 200, 400, 600, 800, and 1000 °C at a low heating rate of 1 °C/min in an electrical furnace. After reaching the target temperature, constant heating was maintained for 1 h to ensure uniform temperature distribution within the sample. After that, the samples were naturally cooled down to ambient temperature inside the furnace. The cooling curve is presented in Fig. 1. Table 3 presents the two different recuring conditions employed. For lime-saturated water (W) recuring, the heated samples were submerged into lime-saturated water for 30 days. For water–CO_2 cyclic (C) recuring, the heated samples were submerged into lime-saturated water for 3 days and then placed in an environmental chamber for 3 days, in which the temperature, the relative humidity, and the concentration of CO_2 were maintained at 30 ± 1 °C, 40 ± 1%, and 20 ± 0.2%, respectively. Low relative humidity was chosen as the diffusivity of CO_2, and carbonation efficiency is favored in an unsaturated micropore solution [28-30]. The two recuring regimes were applied for the same

duration of 30 days. Afterward, the samples were dried for 3 days at a temperature of 45 ± 2 °C and relative humidity of 35 ± 5% before testing.

Table 3. The details of the recuring conditions.

Curing ID	Curing regimes	Solutions	Temperature, relative humidity, and concentration of CO_2	Curing period
W	Continuous full submersion	Lime-saturated water	Natural, environmental, climatic condition	30 days
C	Full submersion with carbonation cycles	Lime-saturated water	30 ± 1 °C, 40 ± 1%, 20 ± 0.2%	(3 + 3) × 5 = 30 days

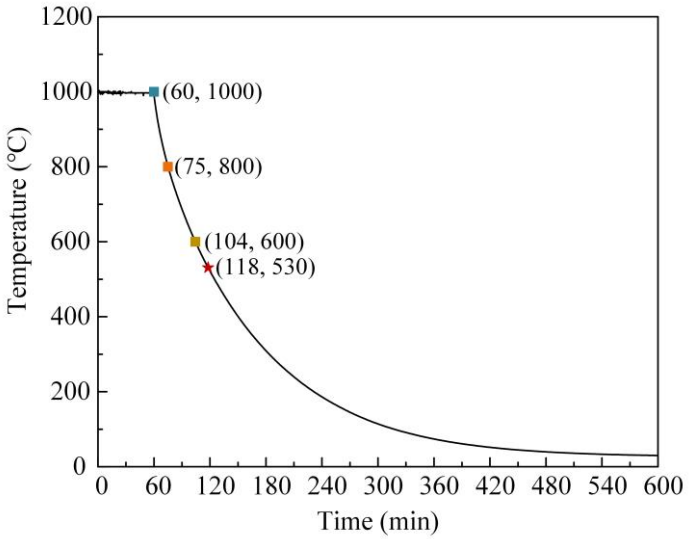

Fig. 1. Cooling curve of the electrical furnace.

2.3. Characterization methods

2.3.1. Compressive strength

The compression tests were conducted at ambient temperature after heating and recuring following ASTM C109/C109M-11 [31]. To this end, a hydraulic compression machine with a capacity of 600 kN driven by a servo-hydraulic control unit was employed. A constant loading rate of 2.4 kN/s was used, and the maximum force was recorded. Three cubic samples were tested for each case to obtain the mean value and standard deviation.

2.3.2. X-ray diffraction

X-ray diffraction analysis was conducted to quantitatively characterize the change in the crystalline phases of the concrete samples before hearting, after heating, and at the end of the recuring. The paste samples were broken into small 5 × 5 × 5 mm^3 pieces and immersed in isopropanol for 24 h to stop hydration and carbonation. Subsequently, the samples were oven-dried at a temperature of 40 °C for 24 h before being ground into powder by pestle and mortar. The Bruker D8 Advance diffractometer with the Cu Kα radiation measured the XRD patterns at 40 kV and 40 mA. The 2θ angle ranged from 5° to 65° at a step size of 0.02° and a scanning rate of 2°/min. Quantitative Rietveld analysis was also carried out utilizing HighScore Plus software according to an external standard strategy.

2.3.3. Thermogravimetric analysis

Thermogravimetric analysis was conducted using NETZSCH STA 449 F5 Jupiter to examine the phase change in the heated and recured samples by measuring the mass loss due to decomposition on heating. The powder samples were prepared using procedures similar to those for the XRD analysis. About 50 mg of the powdered samples was analyzed, and the temperature ranged from 30 to 900 °C at a heating rate of 10 °C/min under a 100 mL/min nitrogen flow.

2.3.4. Scanning electron microscopy and energy-dispersive X-ray spectrometry

Scanning electron microscopy using a Phenom Prox G6 scanning electron microscope, equipped with a backscattered electron imaging detector and energy-dispersive X-ray spectrometry, was utilized to analyze the microstructural changes and elemental composition of the samples. Small 5 × 5 × 5 mm^3 pieces of the HPC samples were cut from the 50 × 50 × 50 mm^3 cubic sample. For the morphological secondary electron analysis, the concrete samples were immersed in 99% isopropanol for 24 h. After oven-drying the samples at a temperature of 40 °C for an extra 24 h, their fractured surface was coated with a gold film to ensure

the adequate conductivity of the electron beam. For the BSE imaging and EDX analysis, the samples were evacuated in a vacuum chamber and impregnated in epoxy resin. After 24 h of hardening, the epoxy-impregnated samples were firstly ground in sequential steps using P320, P800, P1200, and P2000 emery papers. Then, their surface was finely polished using BUEHLER TexMet^{TM} P polishing cloth and 1 µm MetaDi polycrystalline suspension under 20 N loading for 2 min. After polishing, the samples were immediately cleaned by an ultrasonic cleaner in 99% isopropanol and immersed in it for 24 h. Before observation, the samples were oven-dried at 40 °C for another 24 h, and their surface was coated with a thin gold film for 40 s under a vacuum for testing. The images were captured using a BSE imaging detector at a magnification of ×1000 and an acceleration voltage of 15 kV.

2.3.5. Mercury intrusion porosimetry

The mercury intrusion porosimetry measurements using a Micromeritics Autopore IV 9500 porosimeter determined the total porosity and pore size distribution of the HPC samples. The 5 × 5 × 5 mm^3 HPC pieces were produced from the cubic samples. Subsequently, the samples were oven-dried at a temperature of 105 °C for 24 h to eliminate evaporable water. The maximum applied pressure was 227 MPa, covering the pore diameter range of 6 nm to 370 µm.

3. Results

3.1. Compressive strength

Fig. 2 illustrates the compressive strength of the HPC samples after exposure to elevated temperatures. At ambient temperature, the compressive strength of samples 0SF, 0.2SF, and 0.4SF is 83.7, 132.5, and 94.5 MPa, respectively. The presence of silica fume leads to pozzolanic reactions, and the reaction products have favorable cementitious properties and are very efficient in filling up capillary spaces, thereby improving the strength of the samples [32]. However, the excessive addition of silica fume in

sample 0.4SF reduces the fraction of the cement, negatively affecting the compressive strength of this mixture. The exposure of the three mixtures to a temperature of 400 °C significantly increases their compressive strength. Specimen 0.2SF-400 shows the highest compressive strength of 151.8 MPa, followed by specimens 0.4SF-400 and 0SF-400 in sequence. This increase in the compressive strength is attributed to the hydration of anhydrous phases during heating and a lower internal pore pressure during the compression test caused by removing evaporable water from the samples [33, 34]. The formation of both tobermorite ($C_5S_6H_5$) and xonotlite (C_6S_6H) contributes to the further development of the compressive strength of concrete at 400 °C [35]. The compressive strength of the samples starts to decline after exposure to a temperature of 600 °C due to the decomposition of the hydration products, especially the recrystallization of the C–S–H, accompanied by the shrinkage and coarsening of the pore structure [36, 37]. After exposing specimen 0.2SF to a temperature of 800 °C, it maintains the highest residual compressive strength of 64.5 MPa, while the residual compressive strength of samples 0SF-800 and 0.4SF-800 drops to 30.9 and 25.6 MPa, respectively. After heating the HPC samples to 1000 °C, the compressive strength of samples 0/0.2/0.4SF-1000 further decreases to 5.0, 33.0, and 23.0 MPa, respectively.

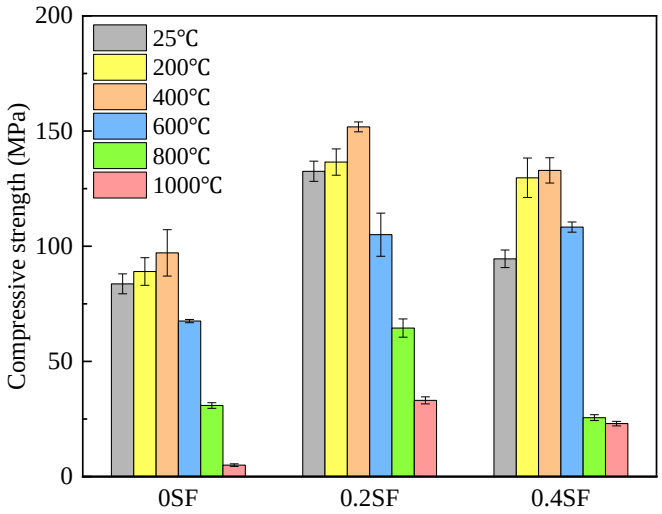

Fig. 2. The compressive strength of the HPC samples after heating at various temperatures.

Fig. 3 delineates the compressive strength of the HPC samples after heating (*H*) and after the recuring. The numbers following the term *SF* indicate the exposure temperature, and the letters *W* and *C* represent the lime-saturated water and water–CO_2 cyclic recuring regimes, respectively. For example, 0.2SF-800-W denotes a sample with a silica fume replacement ratio of 20% exposed to a temperature of 800 °C and recured in lime-saturated water.

After exposing the three mixtures to a temperature of 600 °C, lime-saturated water recuring impacts their compressive strength recovery significantly. Sample 0SF-600-W shows the highest compressive strength recovery of 63.7% (from 67.5 to 110.5 MPa), followed by sample 0.2SF-600-W (from 105.0 to 132.3 MPa) and sample 0.4SF-600-W (from 108.3 to 126.3 MPa). It is worth noting that the recovered compressive strength of samples 0SF-600-W and 0.4SF-600-W after the lime-saturated water recuring even exceeds their respective original compressive strength before heating. The water–CO_2 cyclic recuring also significantly affects the recovery of the compressive strength of the HPC samples, but the influence is slightly weaker than the lime-saturated water recuring.

After exposing samples 0SF and 0.2SF to a temperature of 800 °C, the effect of the lime-saturated water and water–CO_2 cyclic recuring on their compressive strength recovery is remarkable; however, neither of the recuring regimes influences the compressive strength recovery of sample 0.4SF-800. According to Fig. 3b, the compressive strength of sample 0SF-800-W increases by 303.2% from 30.9 to 124.6 MPa, which is 124% of its original compressive strength before heating. Such a substantial improvement in the compressive strength of concrete by recuring has not been reported in the related literature [5, 7, 10, 11, 38, 39]. The compressive strength of sample 0.2SF-800-W also recovers from 64.5 to 107.3 MPa. Similar to the trend observed for the specimens exposed to a temperature of 600 °C, water–CO_2 cyclic recuring shows a slightly lower strength recovery than the lime-saturated water recuring.

The trend of compressive strength recovery is substantially different when the HPC samples are exposed to a temperature of 1000 °C. The water–CO_2 cyclic recuring shows remarkable strength recovery, but the effect of the lime-saturated water recuring is negligible. After water–CO_2 cyclic recuring, the compressive strength of sample 0SF-1000-C increases by more than 15 times from 5.0 to 76.1 MPa after the water–CO_2 cyclic recuring, and the compressive strength of sample 0.2SF-1000-C rises by 67.1 MPa. On the contrary, sample 0.4SF-1000-C shows much lower strength recovery than samples with lower silica content.

In summary, the lime-saturated water recuring has a slightly more profound effect on the compressive strength recovery of HPC than the water–CO_2 cyclic recuring after exposing concrete to a temperature of 600 and 800 °C. However, only the water–CO_2 cyclic recuring is effective after exposing concrete specimens to a temperature of 1000 °C. Samples 0SF and 0.2SF show significant strength recovery after either lime-saturated water or water–CO_2 cyclic recuring, while sample 0.4SF appears less sensitive to recuring. The phase assemblage, chemical composition, microstructural morphology, and porosity of the HPC samples are analyzed in the following sections to examine the mechanism of recuring.

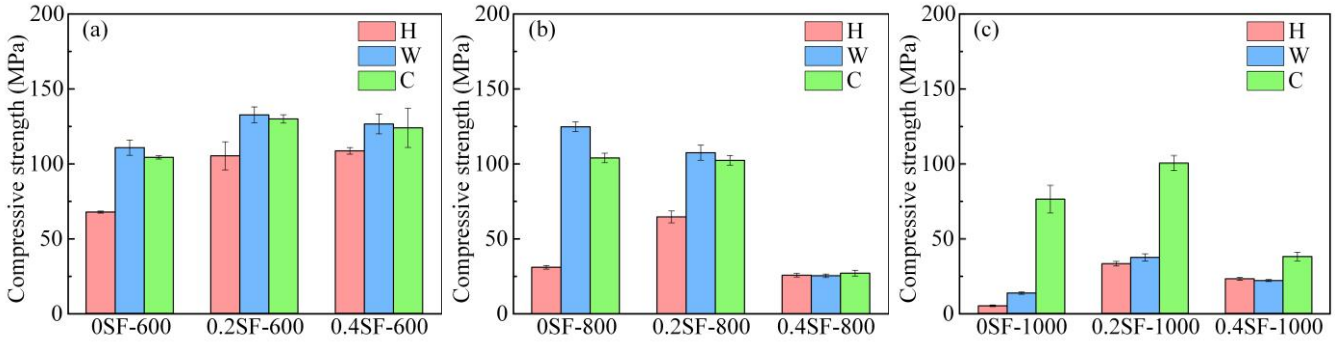

Fig. 3. The compressive strength of the recured HPC samples exposed to a temperature of (a) 600 °C, (b) 800 °C, and (c) 1000 °C.

3.2. Phase assemblage

The HPC phases change after heating and recuring, and the reactivity of the phases after heating directly determines the performance of recuring. Fig. 4 depicts the XRD patterns and Rietveld quantifications of the paste samples before heating. A large quantity of unhydrated cement consisting of Alite (C_3S) and Belite (β-C_2S) remains due to the low water-to-cement ratio, and portlandite (CH) and ettringite (AFt) are the major crystalline hydrated phases. The diffraction peaks of CH decrease with increasing the silica content of samples 0.2SF-25 and 0.4SF-25 due to the initiation of pozzolanic reactions. Although XRD is a good technique for examining crystalline phases, the poorly crystalline phases, such as C–S–H, alumina, ferric oxide, monosulfate (AFm), and unreacted silica fume, can hardly be distinguished from the overall amorphous content.

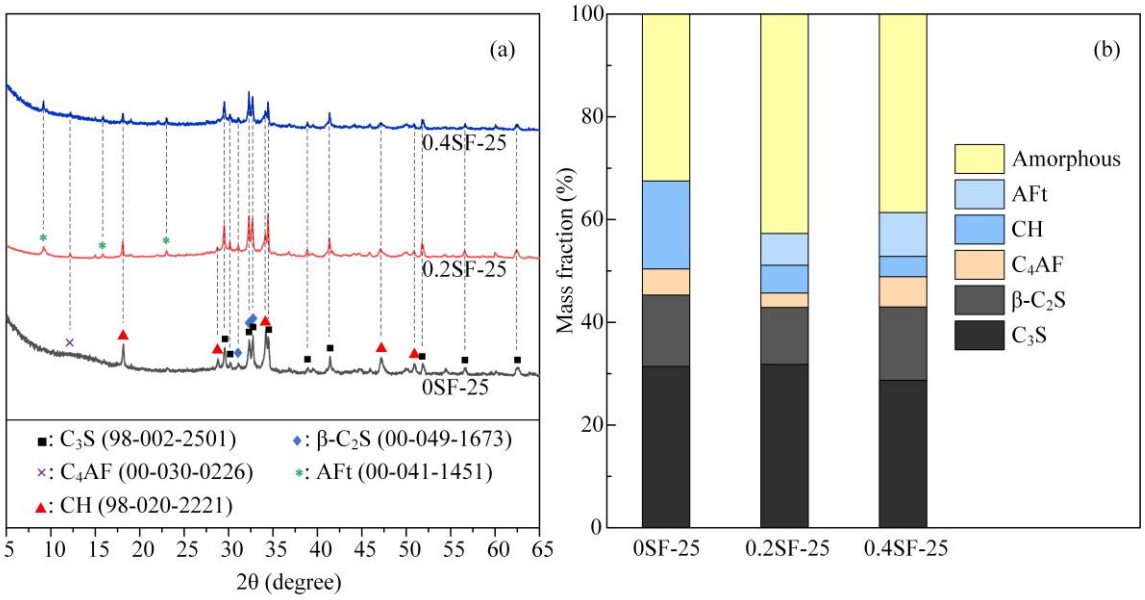

Fig. 4. The XRD results of the paste samples at ambient temperature: (a) the XRD patterns and (b) the Rietveld quantifications.

Fig. 5 shows the XRD results of the samples exposed to a temperature of 600 °C after recuring. Compared to the phase composition of the HPC samples before heating, the unhydrated C_3S and β-C_2S remain unchanged, while the CH and AFt decompose completely at a temperature of 120 °C [40] and 470 °C [41],

respectively. According to previous studies, C–S–H starts to decompose at 500 °C and transforms to β-C_2S at a temperature of around 600 °C [13, 14, 42].

After lime-saturated water recuring, the diffraction peaks associated with C_3S decrease due to the hydration of the unhydrated cement. The amount of β-C_2S, with a lower hydration reactivity, remains constant, and CH is the primary newly formed crystalline phase in sample 0SF-600-W as its diffraction peaks become visible (Fig. 5a). However, no diffraction peak of CH is observed in samples 0.2SF-600-W and 0.4SF-600-W, indicating that CH is consumed by pozzolanic reaction to form C–S–H. As shown in Fig. 5d, the amorphous phases increase in samples 0.2SF-600-W and 0.4SF-600-W.

As shown in Fig. 5d, a large amount of $CaCO_3$ polymorphs is formed as expected because of the carbonation of CH, C–S–H, and calcium silicates. Tetracalcium aluminoferrite (C_4AF) shows a minimal extent of reaction with CO_2 [43]. The depletion of Ca^{2+} ions during carbonation leads to the decalcification of the existing C–S–H and calcium silicates and the formation of amorphous silica gel [44-46], which has a higher density than C–S–H [45, 47]. Sample 0SF-600-C has a lower content of amorphous phases than sample 0SF-600-W, indicating the carbonation of the amorphous phases like C–S–H [48, 49]. For samples 0.2SF-600-C and 0.4SF-600-C, a higher amount of calcium silicates is carbonated to form silica gel. Therefore, the amorphous phases do not decline significantly. Comparing lime-saturated water recuring with water–CO_2 cyclic recuring demonstrates that although the hydration and carbonation processes form completely different new phases, they lead to similar recovery of the compressive strength of the HPC specimens (see Fig. 3).

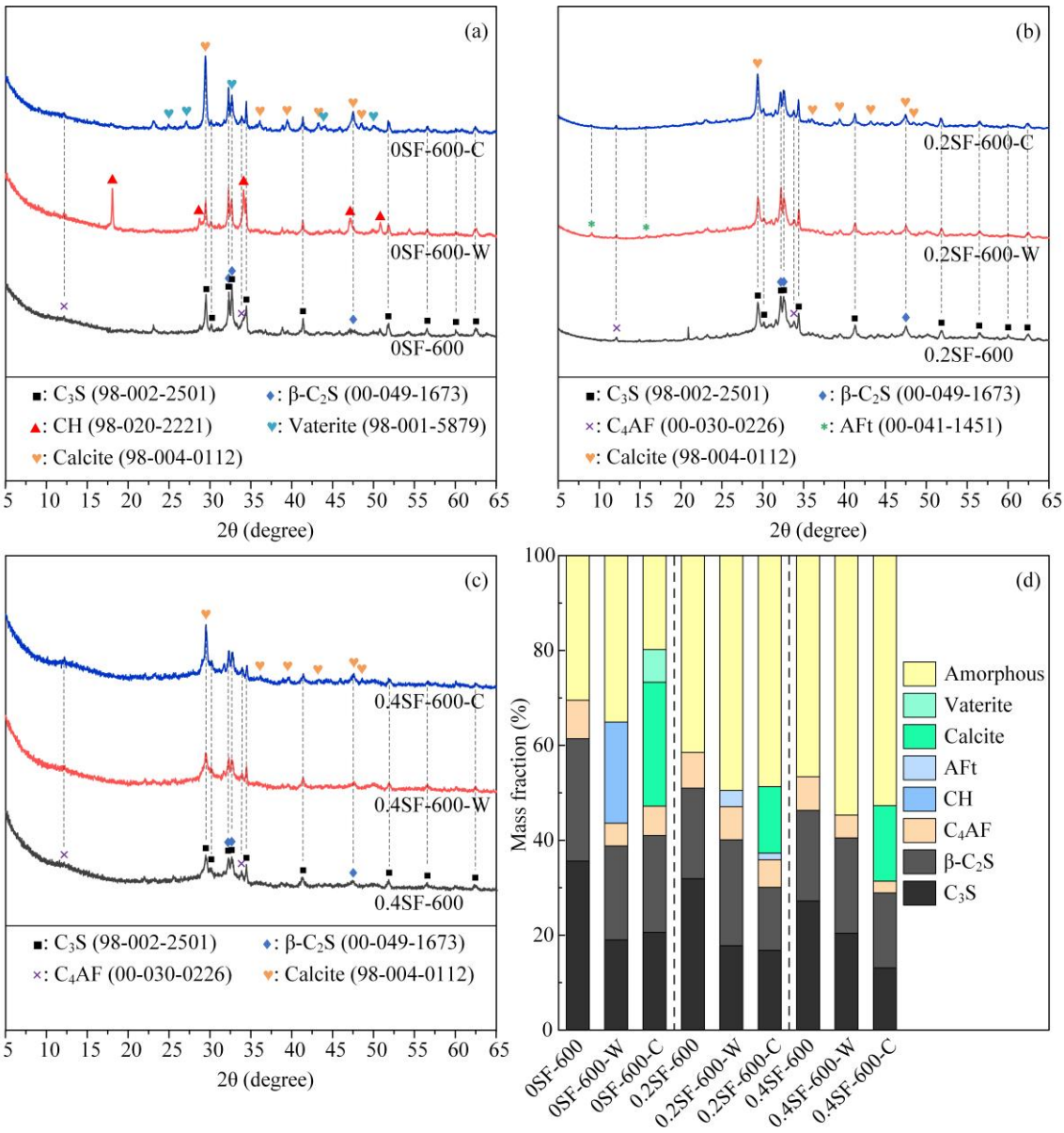

Fig. 5. The XRD results of the specimens exposed to a temperature of 600 °C and the recured HPC samples: (a) the XRD patterns of 0SF samples; (b) the XRD patterns of 0.2SF samples; (c) the XRD patterns of 0.4SF samples; (d) the Rietveld quantifications.

From Fig. 6, the CH, AFt, and a part of the amorphous phases decompose after exposing the high-performance concrete specimens to a temperature of 800 °C. The most notable difference between the three mixtures is the newly formed calcium silicates. C_3S remains in sample 0SF-800, and the decomposition of C–S–H produces a large amount of β-C_2S [37]. For sample 0.2SF-800, C_3S reacts with silica to form calcium silicates with a lower calcium-to-silicon ratio, i.e., β-C_2S, Calcio-olivine (γ-C_2S),

and Wollastonite-2M (CS) [50-52]. The principal peaks of the C_2S polymorphs overlap, so a broad peak is presented at a 2θ angle of 32.5°. The transformation from β-C_2S to γ-C_2S is affected by grain size, internal strain, impurities, and cooling rate. Although "natural cooling" with a furnace is slower than that with air quenching, the full transformation from β-C_2S to γ-C_2S is kinetically restricted. At last, due to the highest silica fume content of sample 0.4SF-800, CS occupies more than 40 wt. % of the sample. The different hydration and carbonation reactivity of these calcium silicate phases strongly affects the recuring performance of the mixtures. After the lime-saturated water recuring, about half of the C_3S and β-C_2S is hydrated in sample 0SF-800-W to form CH and amorphous phases. For sample 0.2SF-800-W, the hydration of the β-C_2S is predominant, but the γ-C_2S and CS remain stable due to their low hydration reactivity. The degree of reaction of the β-C_2S is much higher in sample 0.2SF-800-W than 0.2SF-600-W, which is attributed to the absence of C_3S, the high hydration reactivity of which saturates the pore solution and thus hinders the dissolution of other calcium silicate phases. The β-C_2S in sample 0.4SF-800-W is also hydrated, but fewer hydration products are formed because of its low content. The diffraction peaks of CH are observed in the three samples, but their intensity decreases with increasing the silica fume content of the HPC because of the pozzolanic reaction.

After the water–CO_2 cyclic recuring process, the diffraction peaks of CH are absent. During each carbonation stage, the formed silica gel can act as a pozzolanic material in the subsequent round of hydration in a way similar to a pozzolan to consume CH [53]. As expected, polymorphs of $CaCO_3$, namely vaterite and calcite, are the major constituents of the recured HPC. Although the overall degree of reaction of the calcium silicates increases for sample 0.2SF-800-C compared to 0.2SF-800-W, the corresponding strength recovery of sample 0.2SF-800-C is not higher than that of sample 0.2SF-800-W. Finally, because of the limited reaction of γ-C_2S and CS in sample 0.4SF-800, its strength recovery is negligible after water–CO_2 cyclic curing.

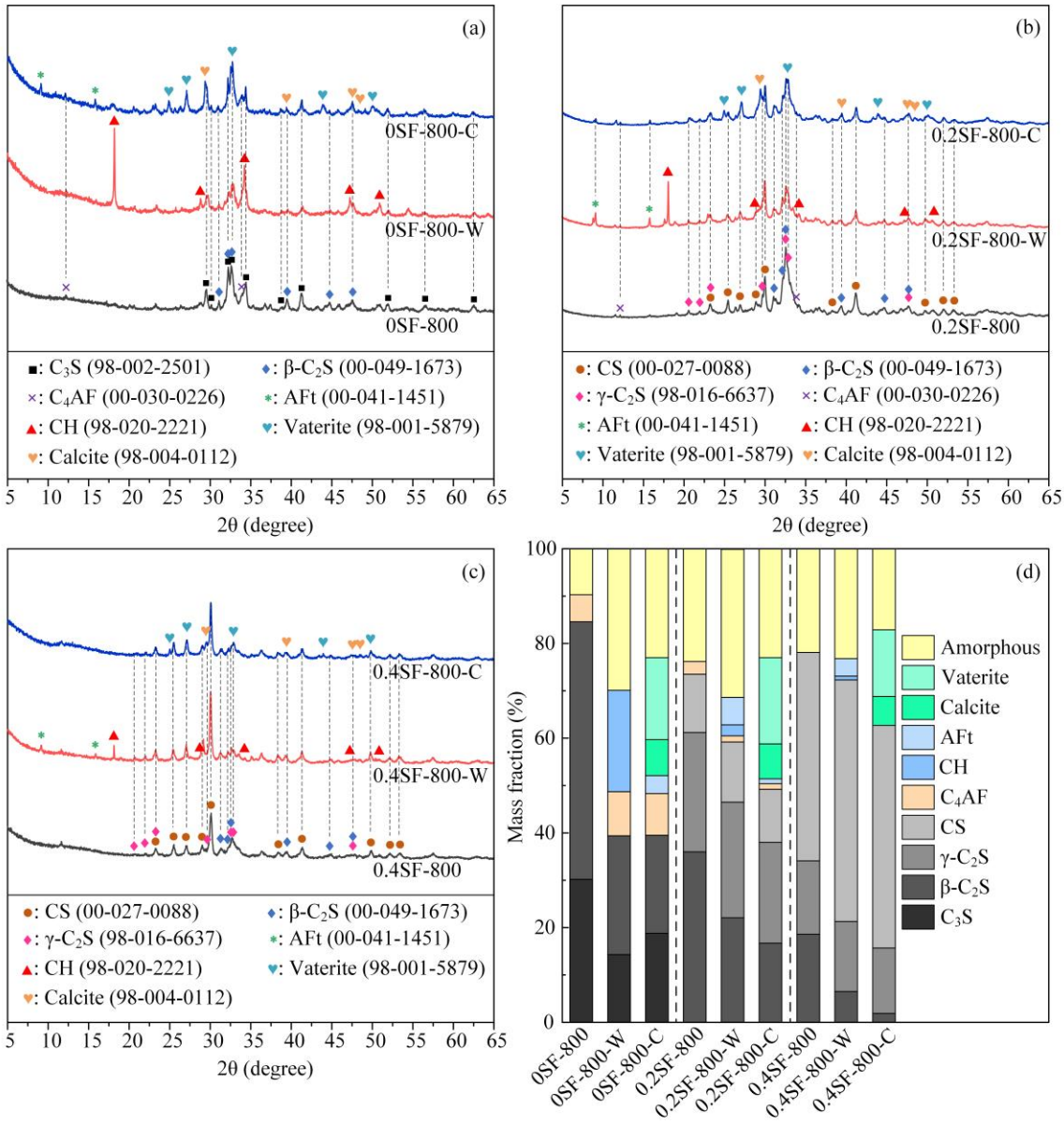

Fig. 6. The XRD results of the specimens exposed to a temperature of 800 °C and the recured HPC samples: (a) the XRD patterns of 0SF samples; (b) the XRD patterns of 0.2SF samples; (c) the XRD patterns of 0.4SF samples; (d) the Rietveld quantifications.

The phase composition of sample 0SF-1000 is similar to that of sample 0SF-800 (Fig. 7), so a similar amount of CH and amorphous phases forms after the lime-saturated water recuring. On the other hand, new phases, namely the rankinite (C_3S_2) and gehlenite (C_2AS), form in sample 0.2SF-1000. Moreover, in sample 0.4SF-1000, CS constitutes around 60% of the total weight of the specimen, followed by C_3S_2 and C_2AS. The C_2AS forms in the solid-state reaction of C_4AF with a high silica content [54]. CS, C_3S_2, and

C_2AS have low water reactivity. Therefore, β-C_2S is the only main phase participating in hydration in sample 0.2SF-1000, and specimen 0.4SF-1000 is barely hydrated.

The water–CO_2 cyclic recuring promotes the reaction of calcium silicates. In sample 0SF-1000-C, almost all the C_3S and about half of the β-C_2S are carbonated to form $CaCO_3$ polymorphs, namely calcite and aragonite. In sample 0.2SF-1000-C, the calcium silicate minerals and amorphous phases are carbonated, and the main $CaCO_3$ formed is calcite. The C_3S_2 and CS phases in sample 0.4SF-1000-C are carbonated despite possessing low hydraulic reactivity, resulting in the formation of calcite and vaterite.

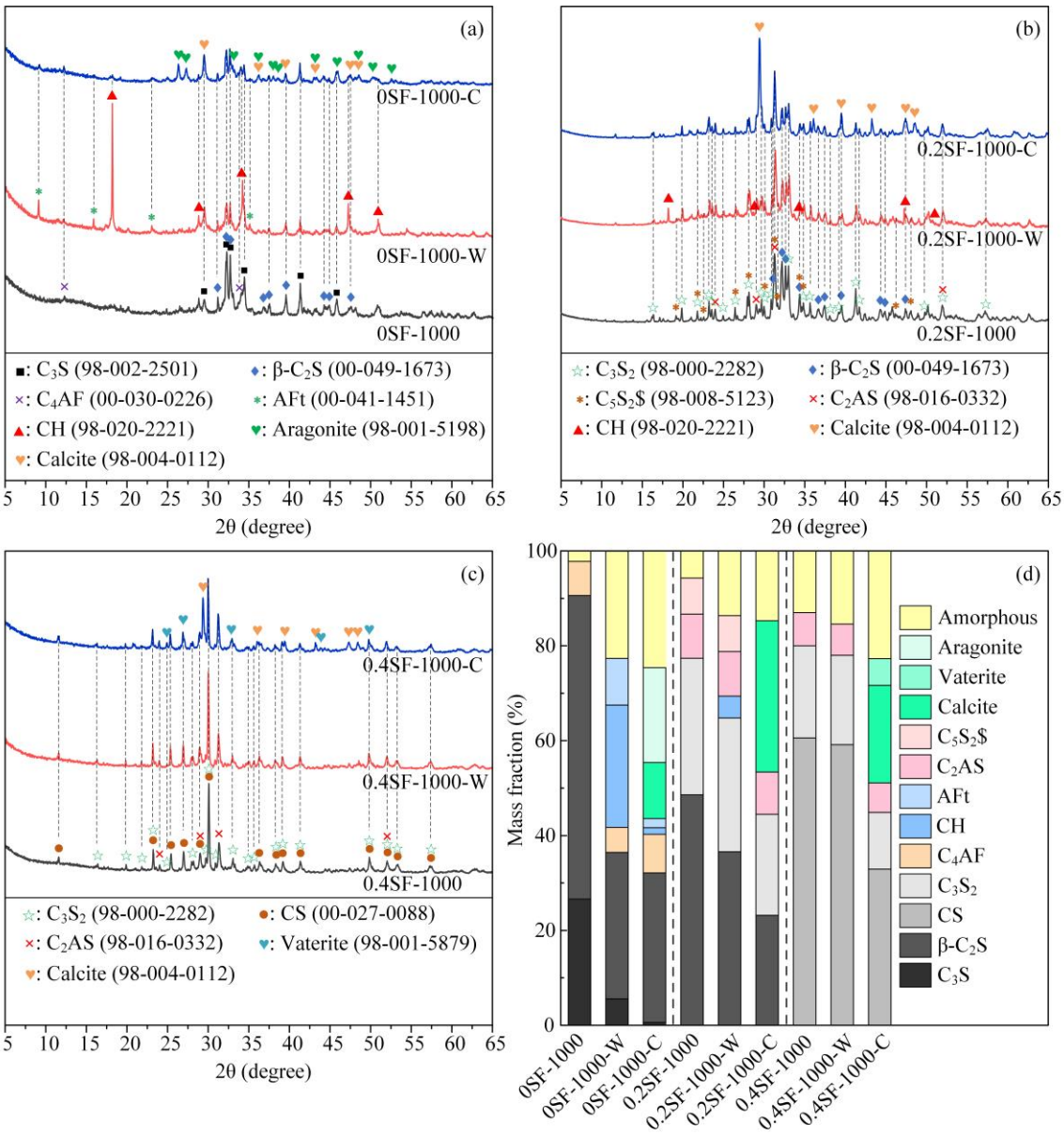

Fig. 7. The XRD results of the specimens exposed to a temperature of 1000 °C and the recured high-performance concrete samples: (a) the XRD patterns of 0SF samples; (b) the XRD patterns of 0.2SF samples; (c) the XRD patterns of 0.4SF samples; (d) the Rietveld quantifications.

Fig. 8 summarizes the phase changes of the HPC during the heating and recuring processes. After exposing the specimens to a temperature of 600 °C, the AFt and CH decompose entirely, while the C_3S and β-C_2S remain intact. The decomposition of C–S–H forms β-C_2S, and solid-state reactions happen at a temperature of 800 and 1000 °C. With the addition of silica, new calcium silicate phases such as γ-C_2S, C_3S_2, and CS form, and C_4AF reacts with silica fume and transforms into C_2AS at a temperature of

1000 °C. The full transformation from β-C_2S to γ-C_2S was kinetically restricted due to the chemical impurities inhibiting the atomic rearrangement necessary to form γ-C_2S [55, 56]. After the lime-saturated water recuring, CH is the main crystalline phase due to the hydration of C_3S and β-C_2S in samples 0SF-600-W, 0SF-800-W, and 0SF-1000-W. Moreover, pozzolanic reactions consume the CH to form C–S–H in samples 0.2SF-600-W, 0.2SF-800-W, 0.4SF-600-W, and 0.4SF-800-W. Other calcium silicate phases, including γ-C_2S, C_3S_2, CS, and C_2AS, generally remain stable due to their low hydration reactivity. After the water–CO_2 cyclic recuring, the hydration products, namely CH, C–S–H, and AFt, are carbonated to form $CaCO_3$ polymorphs and amorphous silica gel. Except for C_3S and β-C_2S, the other calcium silicate phases are also carbonated, and the overall degree of reaction of the calcium silicates improves. During carbonation, the higher undersaturation of Ca^{2+} ions, compared to hydration, accelerates the dissolution rate of the dehydrated products and hence promotes the overall reaction [57, 58]. Carbonation forms the polymorphs of $CaCO_3$, namely calcite, aragonite, and vaterite crystals. According to Cole and Kroone [59], the CO_2 absorbed by mortar and pastes is held by the crystalline forms of vaterite and aragonite that are not as stable as calcite. The formation of vaterite or aragonite is seemingly related to the pH of the pore solution, the presence of highly decalcified C–S–H, and the concentration of ions [45, 46, 60-62]. However, it is difficult to monitor the microenvironment of the HPC samples.

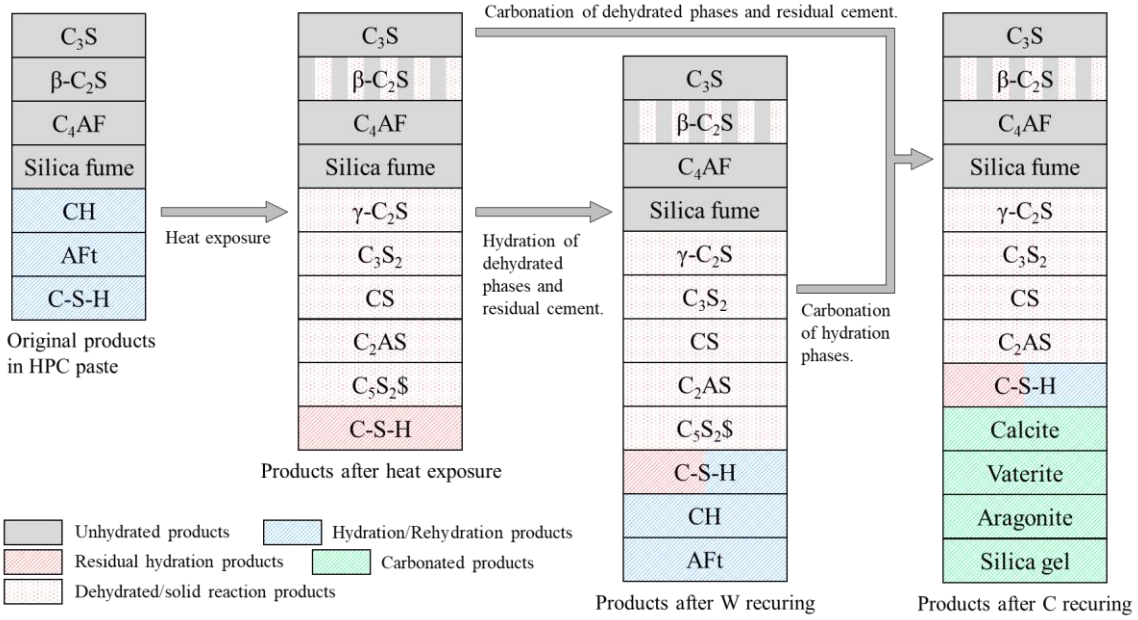

Fig. 8. The summary of the changes in the phases of HPC during the heating and recuring.

3.3. TGA results

Thermogravimetric (TG) analysis provides information on the poorly crystalline phases that are difficult to be analyzed by XRD. Fig. 9 and Fig. 10 delineate the thermogravimetric and differential thermogravimetric (DTG) results of the high-performance concrete samples before heating, after heating, and after recuring. As the DTG curves and the related literature [63] indicate, the mass loss in the temperature range of 50–350 °C is primarily attributed to the dehydration of AFt (at around 115 °C), AFm (below 200 °C), and C–S–H, followed by the dehydroxylation of CH in a temperature range of 350–500 °C. A noticeable mass loss of the carbonated samples can be observed from 500 to 800 °C due to the decomposition of calcium carbonates with different degrees of crystallinity, which is consistent with previous studies [23, 24, 46]. According to Fig. 9, sample 0SF-25 shows an apparent mass loss in a temperature range of 350–500 °C, corresponding to the decomposition of CH. Samples 0.2SF-25 and 0.4SF-25 present slightly higher overall mass loss up to 800 °C than sample 0SF-25 since the pozzolanic reaction increases the degree of hydration.

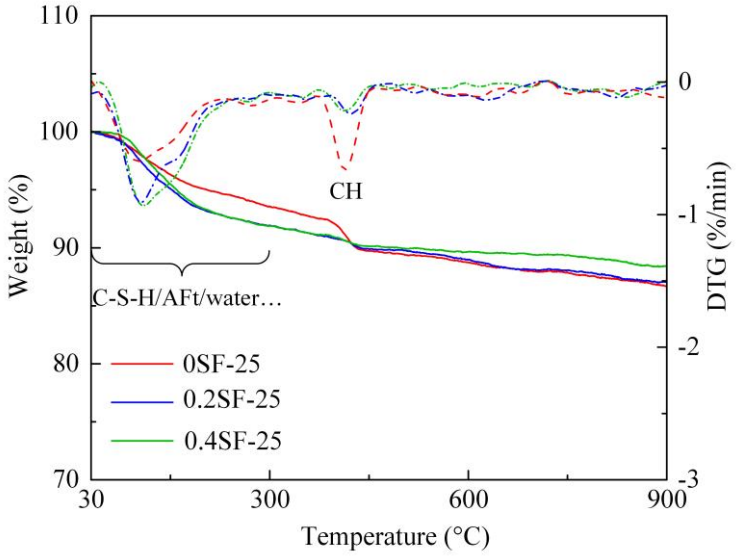

Fig. 9. The thermogravimetric and differential thermogravimetric curves of the HPC samples before heating.

Fig. 10a–c compares the mass loss of the samples after exposure to a temperature of 600 °C and recuring. Noticeable mass loss associated with the decomposition of CH is only observed for sample 0SF-600-W because the CH is carbonated in sample 0SF-600-C and consumed by the pozzolanic reaction in samples 0.2SF-600-W and 0.4SF-600-W. Samples 0SF-600-C and 0.2SF-600-C show a decrease in the mass loss below 350 °C and an increase in mass loss in a temperature range of 500–800 °C compared to samples 0SF-600-W and 0.2SF-600-W because part of the hydration products is carbonated during the water–CO_2 cyclic recuring. This phenomenon is not observed in samples 0.4SF-600-W and 0.4SF-600-C because they have extremely low hydration reactivity. Comparing the three mixtures demonstrates that the degree of carbonation decreases with increasing the silica content, agreeing with the degree of strength recovery shown in Fig. 3.

As shown in Fig. 10d–f, the trend of the mass loss of the HPC exposed to a temperature of 800 °C is similar to that of the samples exposed to a temperature of 600 °C. The hydration products, including CH, are carbonated during the water–CO_2 cyclic recuring, so the mass loss of samples 0SF-800-C and 0.2SF-800-C below 500 °C is lower than that of samples 0SF-800-W and 0.2SF-800-W respectively. As the

XRD results indicate, the dehydration products of sample 0.4SF-800 are mainly nonhydraulic. Therefore, sample 0.4SF-800-W exhibits negligible mass loss after the lime-saturated water recuring. For the three mixtures, carbonation during the water–CO_2 cyclic recuring enhances the reaction of the dehydration products and thus increases their respective overall mass losses. A notable difference in the TGA results of the samples exposed to a temperature of 1000 °C is that sample 0.2SF-1000-W shows a much lower mass loss than samples 0.2SF-600-W and 0.2SF-800-W. However, after carbonation, its mass loss in a temperature range of 500–800 °C is higher than that of samples 0.2SF-600-C and 0.2SF-800-C.

For all the carbonated HPC samples, the co-existence of $CaCO_3$ crystals and poorly crystalline $CaCO_3$ makes it challenging to distinguish the mass loss corresponding to the decomposition of each phase in a temperature range of 500–800 °C [45, 48, 64, 65]. Refs [66-68] reported similar results for the carbonated cement pastes. Thiery et al. [61] proposed three temperature ranges for the decomposition of $CaCO_3$ polymorphs. The mass loss in a temperature range of 550–680 °C is related to the decomposition of amorphous $CaCO_3$ with low thermodynamic stability, and the vaterite and aragonite decompose at higher temperatures between 680 and 780 °C. Finally, well-crystallized calcite supposedly decomposes in a temperature range of 780–990 °C. The related literature indicates that the local concentration of CO_2 [68], pH of the associated solution [45], and space for dissolution–precipitation processes affect the crystallinity of calcium carbonate. During the carbonation of the C–S–H or AFt/AFm phases with a high concentration of silicon [53, 69, 70] or when the degree of carbonation is relatively high at CO_2 concentrations up to 10% [69], poorly crystalline $CaCO_3$ forms, extending the corresponding mass loss even to low temperatures of about 250 °C [45, 48, 61, 69, 71]. Brečević [72] indicated that the amorphous $CaCO_3$ compounds form when the pH value of the pore solution is below nine, which is possible when the concentration of CO_2 and the carbonation level rise. At last, the formation of poorly crystalline $CaCO_3$ improves in the limited space, retarding its transformation into thermodynamically stable calcite formed by the dissolution–

precipitation process [63, 73]. However, the origin of the formation of the metastable amorphous calcium carbonate is not thoroughly understood [74].

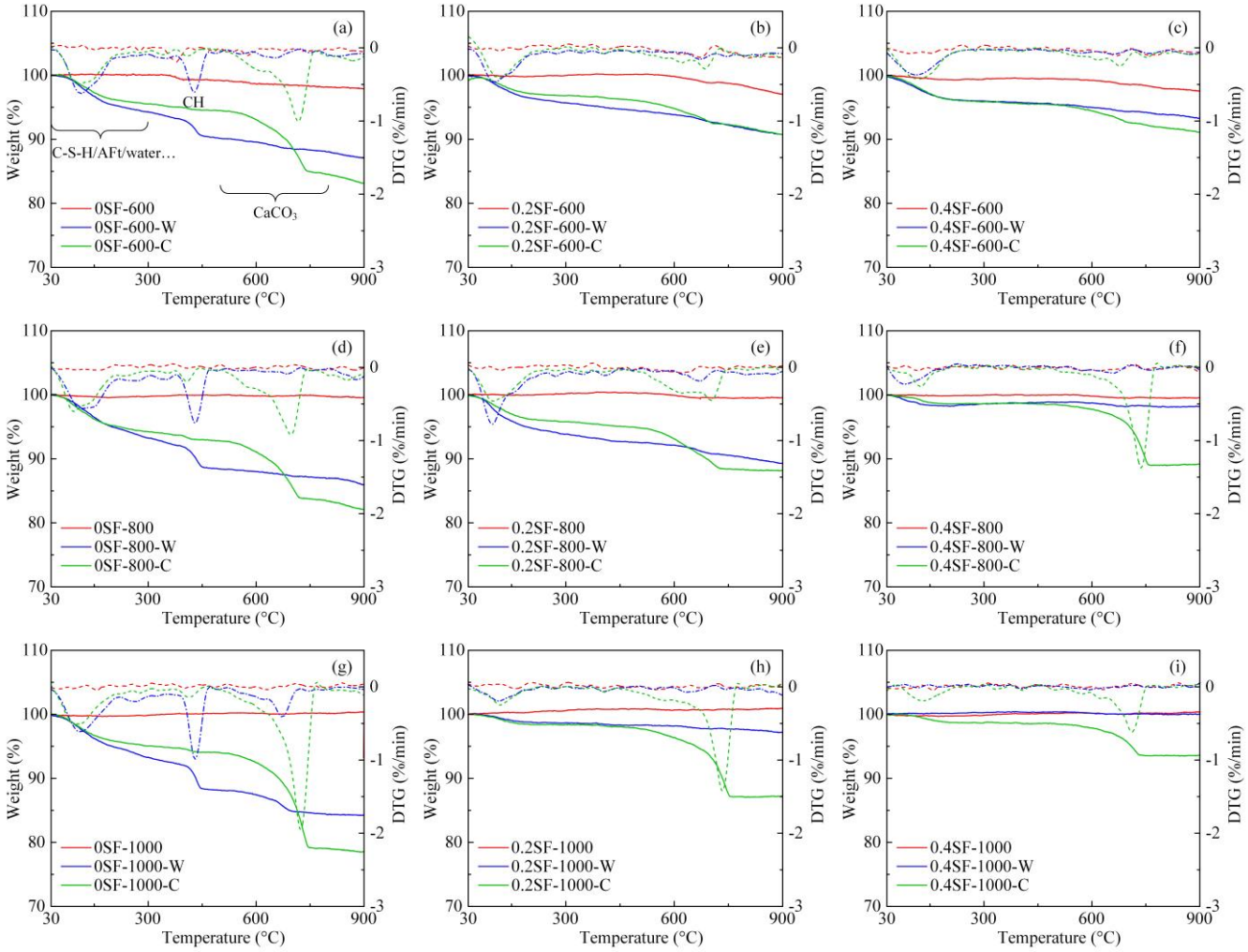

Fig. 10. The thermogravimetric and differential thermogravimetric curves of the HPC samples after heating and recuring: (a–c) after exposure to a temperature of 600 °C and recuring; (d–f) after exposure to a temperature of 800 °C and recuring; (g–i) after exposure to a temperature of 1000 °C and recuring.

The XRD and TG results presented in Sections 3.2 and 3.3 confirm that carbonation accelerates the reaction of the calcium silicates since a less amount of calcium silicates remain and more $CaCO_3$ forms after the water–CO_2 cyclic recuring. This phenomenon is explained by the fact that dissolving CO_2 in the pore solution causes the undersaturation of the anhydrous calcium silicates in the pore solution [75], which facilitates the dissolution of the calcium silicates [58]. Previous studies have reported that belite reacts

faster than alite during carbonation [66, 74, 76]. Nevertheless, the overall degree of reaction of C_3S is higher than that of β-C_2S and γ-C_2S in the present study, attributed to the cyclic curing regime in the water–CO_2 cyclic recuring. C_3S is dissolved faster during the water submersion stage due to its higher solubility [77]. The high ion concentration of the pore solution retards the dissolution of β-C_2S and thus the hydration reaction. In the carbonation stage, the CH reacts with the dissolved CO_2 first, buffering the carbonation of C_3S and β-C_2S. Therefore, the higher carbonation rate of β-C_2S than C_3S cannot be manifested.

3.4. Microstructure observations

Scanning electron microscopy examined the microstructural changes of the samples exposed to elevated temperatures and recured. The BSE imaging mode was used to detect different phases since grayscale in BSE images is primarily a function of the mean atomic number [78]. Images in the secondary electron imaging (SEI) mode were also taken to present the local morphology of the samples. As shown in Fig. 11, the microstructure of sample 0SF-25 is compact due to its low water-to-binder ratio. Samples 0.2SF-25 and 0.4SF-25 offer a denser microstructure due to the pozzolanic reaction between CH and silica fume [18, 79] and the filling effect of silica fume. As labeled in Fig. 11b, the large and homogeneous objects are sand particles. In the region of the cement paste, the brighter areas are unhydrated cement grains, the hydration products primarily occupy the gray part, and the dark areas represent pores or microcracks.

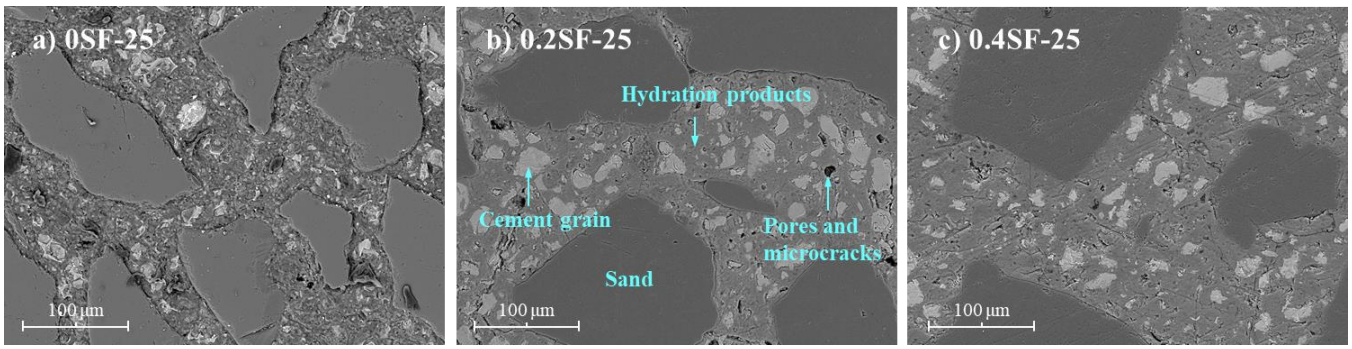

Fig. 11. The microstructure of the three mixtures before being heated: (a) 0SF; (b) 0.2SF; (c) 0.4SF.

Fig. 12 presents the microstructure of the HPC samples after being exposed to a temperature of 600 °C and recuring. According to Fig. 12a, sample 0SF-600 exhibits slight coarsening of the hydration products, while no microcrack is observed. On the contrary, many microcracks are generated in samples 0.2SF-600 and 0.4SF-600 with the addition of silica fume. Additionally, it appears that microcracks in sample 0.4SF-600 are broader than those in sample 0.2SF-600. The XRD results and the related literature demonstrate that exposing concrete to a temperature of 600 °C gives rise to volume-changing processes, including the dehydration and recrystallization of C–S–H [37, 80], the decomposition of CH, and the phase transformation of quartz sand [80, 81]. The higher stiffness of the cement pastes in samples 0.2SF-600 and 0.4SF-600 causes higher thermal stress and thus leads to the generation of microcracks [82, 83].

After the lime-saturated water recuring, the rehydration products form throughout the cement pastes of the three samples. Platelike CH crystals can be observed in sample 0SF-600-W filling the coarsened pore structure (see Fig. 12d). For samples 0.2SF-600-W and 0.4SF-600-W, the densification of the cement paste is mainly attributed to the formation of amorphous phases, as demonstrated by the XRD results. Microcracks in samples 0.2SF-600-W and 0.4SF-600-W are significantly narrowed due to the expansion of the dehydrated phases with rehydration and relative humidity recovery [84, 85]. Moreover, the newly formed AFt partially fills the microcracks in sample 0.2SF-600-W.

The water–CO_2 cyclic recuring densifies the cement pastes. Intermixing of cubical calcite with rod-shaped vaterite crystals can be observed in sample 0SF-600-C. After the water–CO_2 cyclic recuring, the most noticeable change is filling microcracks with newly formed $CaCO_3$ crystals in samples 0.2SF-600-C and 0.4SF-600-C. During the carbonation stage of the water–CO_2 cyclic recuring, the evaporation of moisture results in the supersaturation of the pore solution. Thus, Ca^{2+} ions precipitate in pores and microcracks from the solution accompanied by carbonation due to the ingress of CO_2. The zoomed inset in Fig. 12h shows that $CaCO_3$ crystals grow from both sides of the microcrack, and a crevice smaller than 1 μm is left

in the microcrack. In summary, the lime-saturated water and water–CO_2 cyclic recuring regimes densify the cement pastes and narrow or fill the microcracks of the thermally damaged samples, thereby recovering their compressive strength.

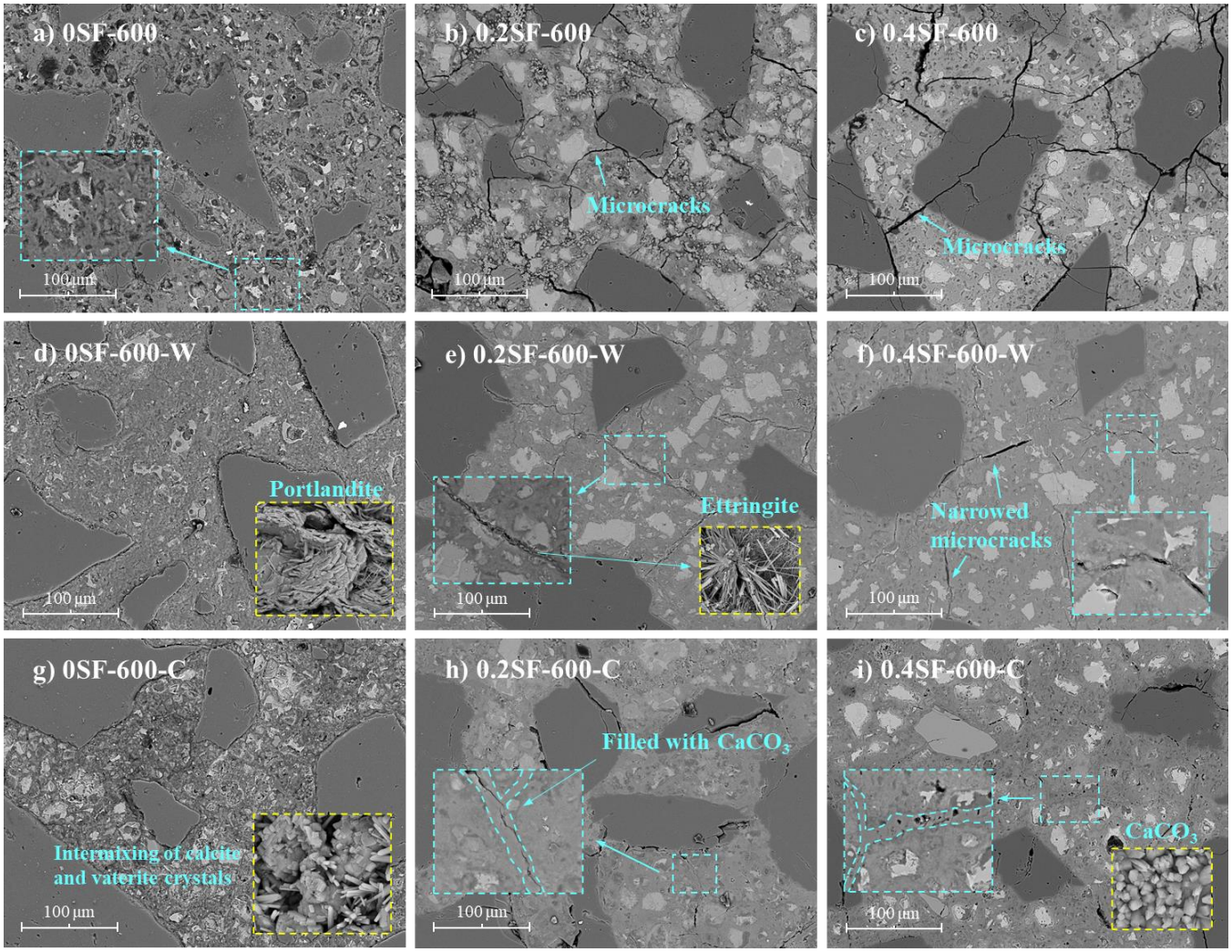

Fig. 12. The microstructure of the HPC samples after (a–c) exposure to a temperature of 600 °C, (d–f) the lime-saturated water recuring, and (g–i) the water–CO_2 cyclic recuring.

Exposing the HPC samples to a temperature of 800 °C gives rise to the further decomposition of their hydration products [86]. The cement paste in sample 0SF-800 exhibits a highly loose and porous microstructure (see Fig. 13a). Although the microcracks are not quantified, they appear wider in samples 0.2SF-800 and 0.4SF-800 compared to the corresponding samples exposed to a temperature of 600 °C,

which is ascribed to the substantial volume change during the decomposition of C–S–H and the transformation of the calcium silicate phases above 600 °C [37, 52].

After the lime-saturated water recuring, large pores can still be observed in sample 0SF-800, while the cement paste appears denser and more homogeneous. CH crystals are widely observed in the SEI mode (see Fig. 13d). In sample 0.2SF-800-W, needle-shaped AFt crystals and amorphous phase can be observed on the fractured surface (see Fig. 13e), which agrees with the XRD and TGA results, indicating the leaching of SO_4^{2-} from the bulk paste into the microcracks. On the other hand, neither the cement paste nor the microcracks are effectively healed in sample 0.4SF-800-W (Fig. 13f).

The water–CO_2 cyclic recuring densifies the bulk cement paste of the three mixtures since a large amount of $CaCO_3$ polymorphs is identified. As shown in the XRD results (Fig. 6), a large part of the decomposed hydration products transform into β-C_2S in sample 0.2SF-800, which is consumed to form $CaCO_3$ crystals; thus, the microcracks are healed during the water–CO_2 cyclic recuring (Fig. 13h). On the contrary, the main dehydration product in sample 0.4SF-800 is CS that remains stable during the water–CO_2 cyclic recuring. The carbonation of the low amount of residual β-C_2S in sample 0.4SF-800 only repairs the surrounding area of the cement particles but leaves the microcracks unfilled.

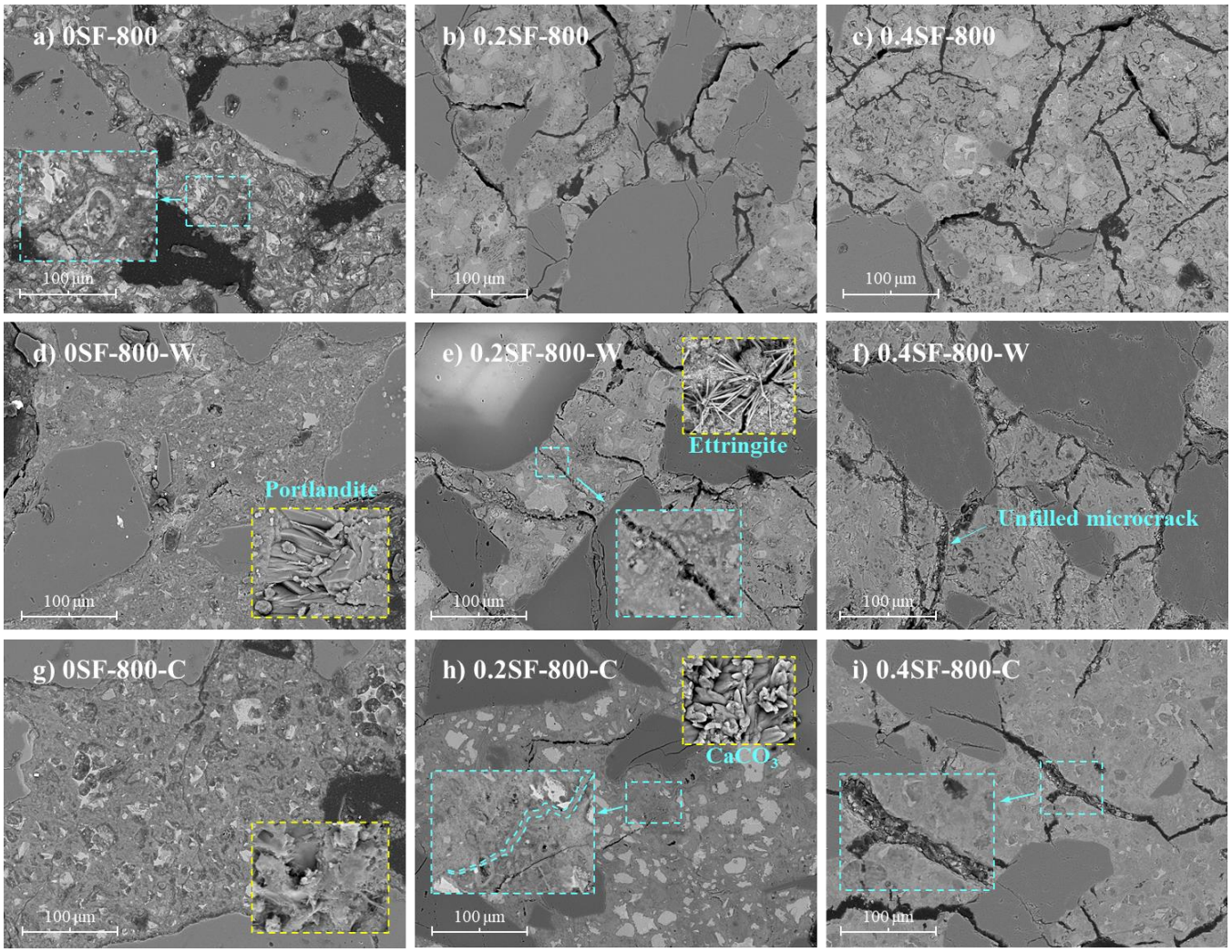

Fig. 13. The microstructure of the HPC samples after (a–c) exposure to a temperature of 800 °C, (d–f) the lime-saturated water recuring, and (g–i) the water–CO_2 cyclic recuring.

Fig. 14 illustrates the microstructure of the HPC samples after being exposed to a temperature of 1000 °C and recuring. A noticeable change is that the cement grains and hydration products cannot be distinguished due to the solid-state reaction. According to Fig. 14a, sample 0SF-1000 has a foam-like structure with agglomerated particles. The boundary of the sand particles exhibits a crystalline structure, indicating the reaction of the hydration products with the sand particles. The microstructure of sample 0.2SF-1000, with a disintegrated cement paste and microcracks, is also very porous (see Fig. 14b). The bulk cement paste of sample 0.4SF-1000 appears to be the densest, but the microcracks are much wider (Fig. 14c).

Although the XRD detected CH and AFt in sample 0SF-1000-W, its microstructure is still porous and poorly cohesive, with a weak bond between the particle agglomerates (see Fig. 14d). The cement paste of samples 0.2SF-1000-W and 0.4SF-1000-W does not show significant densification, and poorly consolidated AFt crystals sporadically form inside the wide microcracks. Further, the needles grow in a radial pattern with a loose structure (Fig. 14e and f) and are not detected by the XRD analysis due to their low amount. Under the competing effects of filling-up and expansion of AFt crystals, the compressive strength recovery of the HPC specimens is negligible after the lime-saturated water recuring.

In contrast to the observations after the lime-saturated water recuring, the water–CO_2 cyclic recuring has a significant healing effect on the microstructure of the HPC samples. The cement pastes are significantly densified by forming a large quantity of $CaCO_3$ crystals. The clavate aragonite crystals can be observed on the fracture surface of sample 0SF-1000-C (Fig. 14g), and microcracks in sample 0.2SF-1000-C are partially filled with short, rod-shaped calcite crystals (Fig. 14h). The zoomed inset in Fig. 14h demonstrates that the $CaCO_3$ crystals grow from the foam-like skeleton of the dehydrated cement paste. Eventually, the loose microstructure coalesces. The microcracks in sample 0.4SF-1000-C appear narrower after the water–CO_2 cyclic recuring although they are not well filled (Fig. 14i). In general, the water–CO_2 cyclic recuring shows much better strength recovery than the lime-saturated water recuring for the HPC samples exposed to a temperature of 1000 °C.

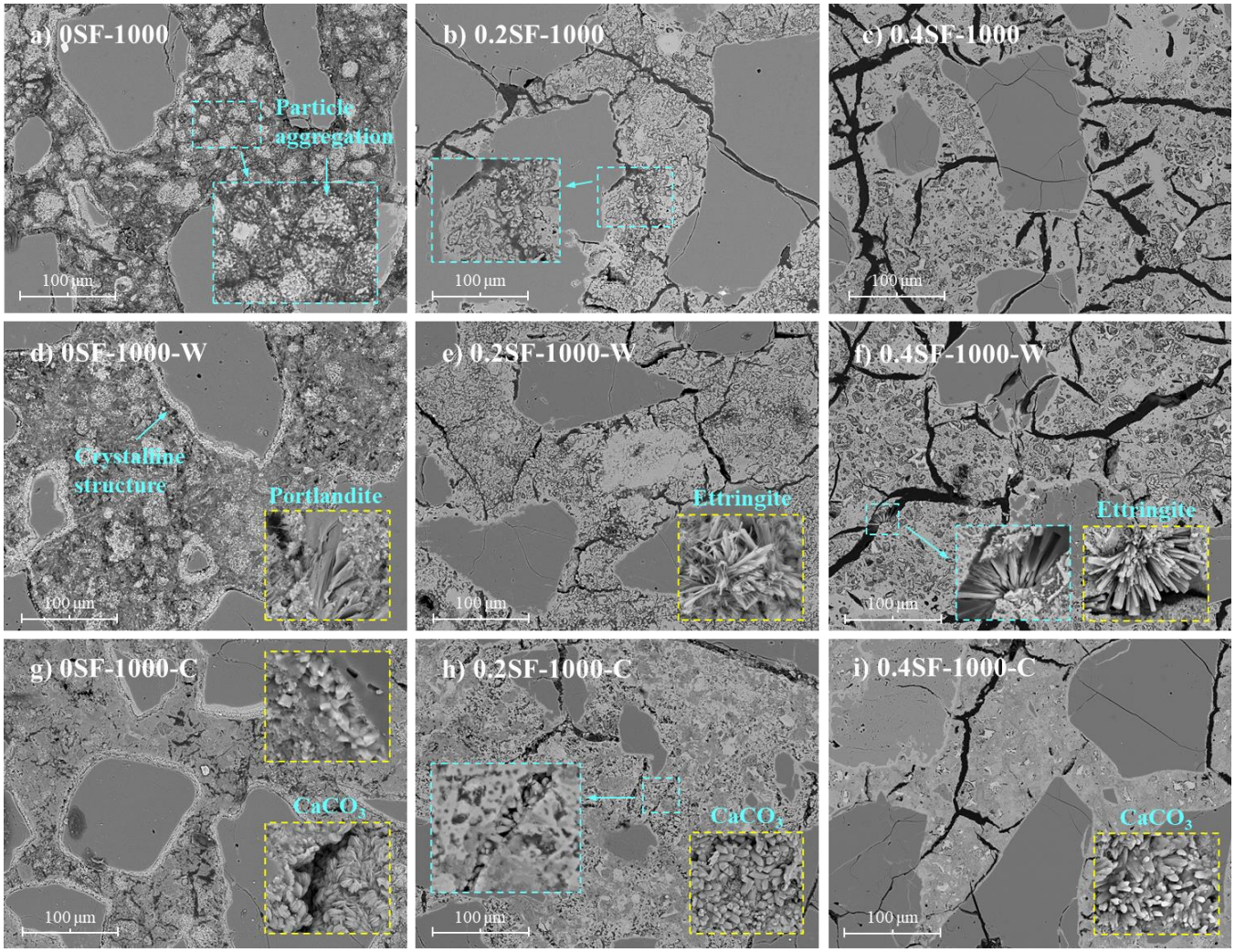

Fig. 14. The microstructure of the HPC samples after (a–c) exposure to a temperature of 1000 °C, (d–f) the lime-saturated water recuring, and (g–i) the water–CO_2 cyclic recuring.

3.5. EDX results

The energy-dispersive X-ray spectrometry measurements determined the atomic ratios of silicon to calcium (Si/Ca) and aluminum plus iron to calcium ((Al+Fe)/Ca) of the different phases of the polished HPC samples. Hence, the phase distribution and ionic migration after the recuring can be further clarified. Fig. 15 illustrates the locations of the collected EDX points. The points of the HPC samples exposed to a temperature of 600 and 800 °C are collected in the areas occupied by the cement grains and hydration products. In the cement grains, the brighter calcium ferro-aluminate is called C_4AF-cement, while the darker calcium silicate is called C_xS_y-cement. After exposing the cement paste to a temperature of 1000 °C,

the cement grains and hydration products cannot be distinguished (Fig. 15b). Moreover, the surrounding regions of the sand particles are referred to as the interfacial transition zones (ITZs) due to their distinctive morphology. It is worth mentioning that the CH, $CaCO_3$, and AFt formed inside microcracks are pretty certain, and thus the results are not presented. Around 700 points are collected in the HPC samples: 24 points for each of the samples exposed to 600 and 800 °C and 30 points for each of the samples exposed to 1000 °C.

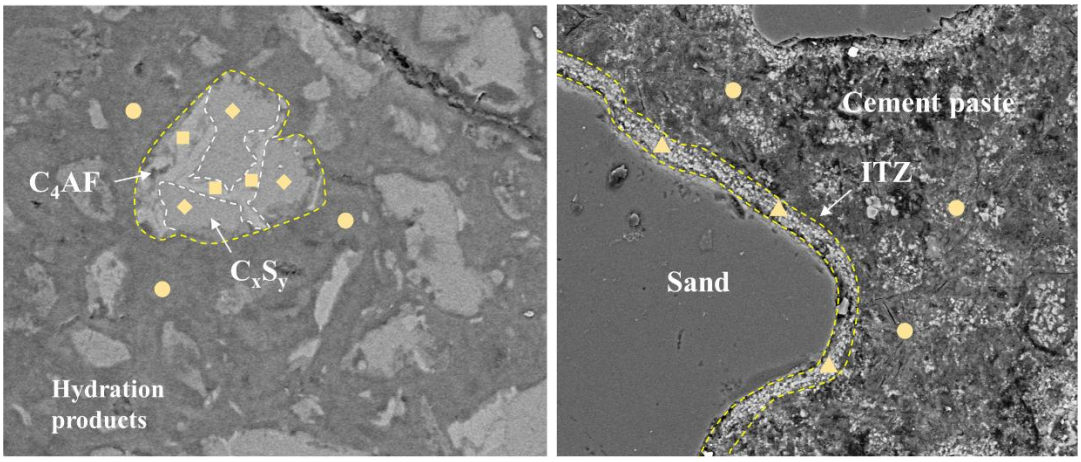

C_4AF-cement (▫); C_xS_y-cement (◇); hydration products (○); the interfacial transition zones of sand particles (△)

Fig. 15. The point selection in the energy-dispersive X-ray spectrometry measurements: (a) before heating and after exposing the HPC samples to a temperature of 600 and 800 °C; (b) after exposing the HPC samples to a temperature of 1000 °C.

Fig. 16–Fig. 19 present the EDX results of the samples by plotting the atomic Si/Ca against the atomic (Al+Fe)/Ca. The dashed lines are drawn using the theoretical C–S–H points to the different phases with specific theoretical compositions. On the basis of the atomic ratio of silicon to calcium, the hydration products are assigned to three microstructural compositions. The first composition associated with an atomic Si/Ca between 0.50 and 0.67 is classified as the regular C–S–H in the hydrated samples [87-89] or a composite phase combining calcium-modified silica and $CaCO_3$ in a carbonated cementitious system [23]. The second composition with an atomic Si/Ca lower than 0.50 is identified to be CH or $CaCO_3$ after carbonation, although it may contain a low amount of silica as well. The third composition with an atomic Si/Ca higher than 0.67 is considered unreacted silica fume and calcium-modified silica gel [23].

Fig. 16 presents the EDX results of the three mixtures before heating. A significant number of points are well aligned toward the pole of C_4AF, indicating its low reaction rate. The C_xS_y-cement exhibits two clusters with an Si/Ca of 0.30 and 0.43, associated with the unhydrated C_3S and C_2S, respectively. The Si/Ca of the hydration products rises with increasing the silica fume content in samples 0SF-25, 0.2SF-25, and 0.4SF-25. The Si/Ca of the hydration products of sample 0SF-25 varies considerably from 0.40 to 0.73, indicating an intermixing of C–S–H with microcrystalline CH, following the XRD results (see Fig. 4). The high value of its (Al+Fe)/Ca implies the hydration of tricalcium aluminate (C_3A) and the existence of C–A–S–H submicronic mixture. The hydration products of sample 0.2SF-25 have a higher Si/Ca between 0.50 and 0.69, indicating a total consumption of CH in pozzolanic reaction and the formation of further C–S–H. The hydration products of sample 0.4SF-25 show the highest Si/Ca due to a large amount of unreacted or partially reacted silica fume agglomerate.

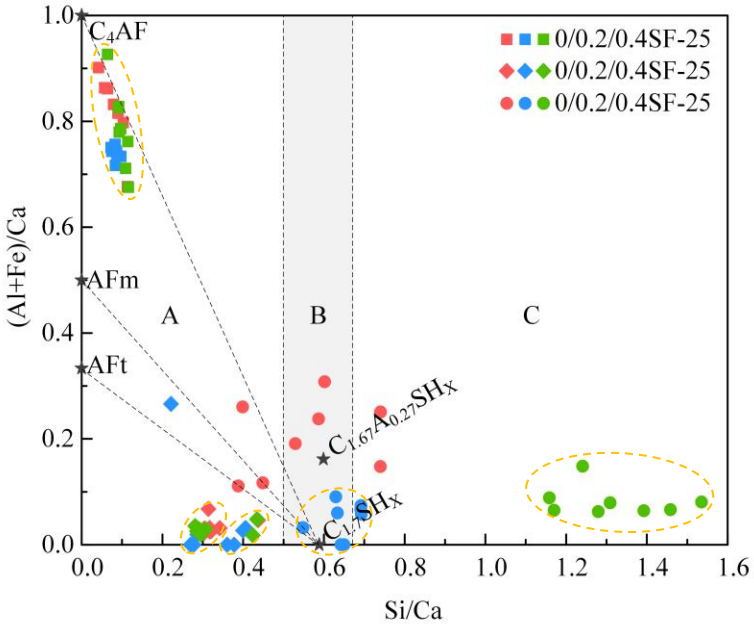

A: $CH/CaCO_3$; B: C–S–H/Intermixing of calcium-modified silica with $CaCO_3$; C: unreacted silica fume/calcium-modified silica.

Fig. 16. The molar (Al+Fe)/Ca as a function of the molar Si/Ca of the HPC samples before being heated.

Fig. 17 delineates the variation in the atomic (Al+Fe)/Ca as a function of the atomic Si/Ca for the three mixtures after being exposed to a temperature of 600 °C and recuring. Exposing the HPC samples to a

temperature of 600 °C does not noticeably change the atomic (Al+Fe)/Ca and Si/Ca in the area of the cement grain consisting of C_4AF-cement and C_xS_y-cement. The silica content of the HPC samples also determines the atomic Si/Ca of the hydration products.

The lime-saturated water recuring does not affect the composition of the C_4AF-cement. Points in the C_xS_y-cement area of sample 0SF-600-W show an increase in Si/Ca and (Al+Fe)/Ca, initiating the dissolution of the cement grains and precipitation of the rehydration products in this area. On the contrary, the corresponding Si/Ca of samples 0.2SF-600-W and 0.4SF-600-W remains unchanged, which agrees with the BSE imaging observation, implying that the boundary of the cement grains is clear (see Fig. 12e and f). The rehydration products of sample 0SF-600-W show a low atomic Si/Ca (0.32–0.42) but a relatively high atomic (Al+Fe)/Ca (0.09–0.42), indicating an intermixing of CH with aluminates. On the other hand, the rehydration products of sample 0.2SF-600-W contain a large quantity of C–S–H intermixed with silica fume (an Si/Ca of 0.58–0.93), and sample 0.4SF-600-W has a very high silica content (an Si/Ca of 0.93–1.44).

After the water–CO_2 cyclic recuring, the C_4AF remains stable in the three mixtures. The atomic Si/Ca of the C_xS_y-cement area of sample 0SF-600-C varies considerably from 0.33 to 0.79, while the Si/Ca of samples 0.2SF-600-C and 0.4SF-600-C remains stable. The replacement ratio of silica fume primarily determines the Si/Ca of the rehydration products. Thus, a low value of the Si/Ca of sample 0SF-600-C in the range of 0.27–0.32 indicates the prevalence of $CaCO_3$, and the medium value of the Si/Ca of sample 0.2SF-600-C in the range of 0.46–0.80 is attributed to intermixing of carbonated C–S–H with calcium-modified silica. At last, the highest Si/Ca of sample 0.4SF-600-C in the range of 1.0–1.23 is ascribed to the calcium-modified silica and unreacted silica fume.

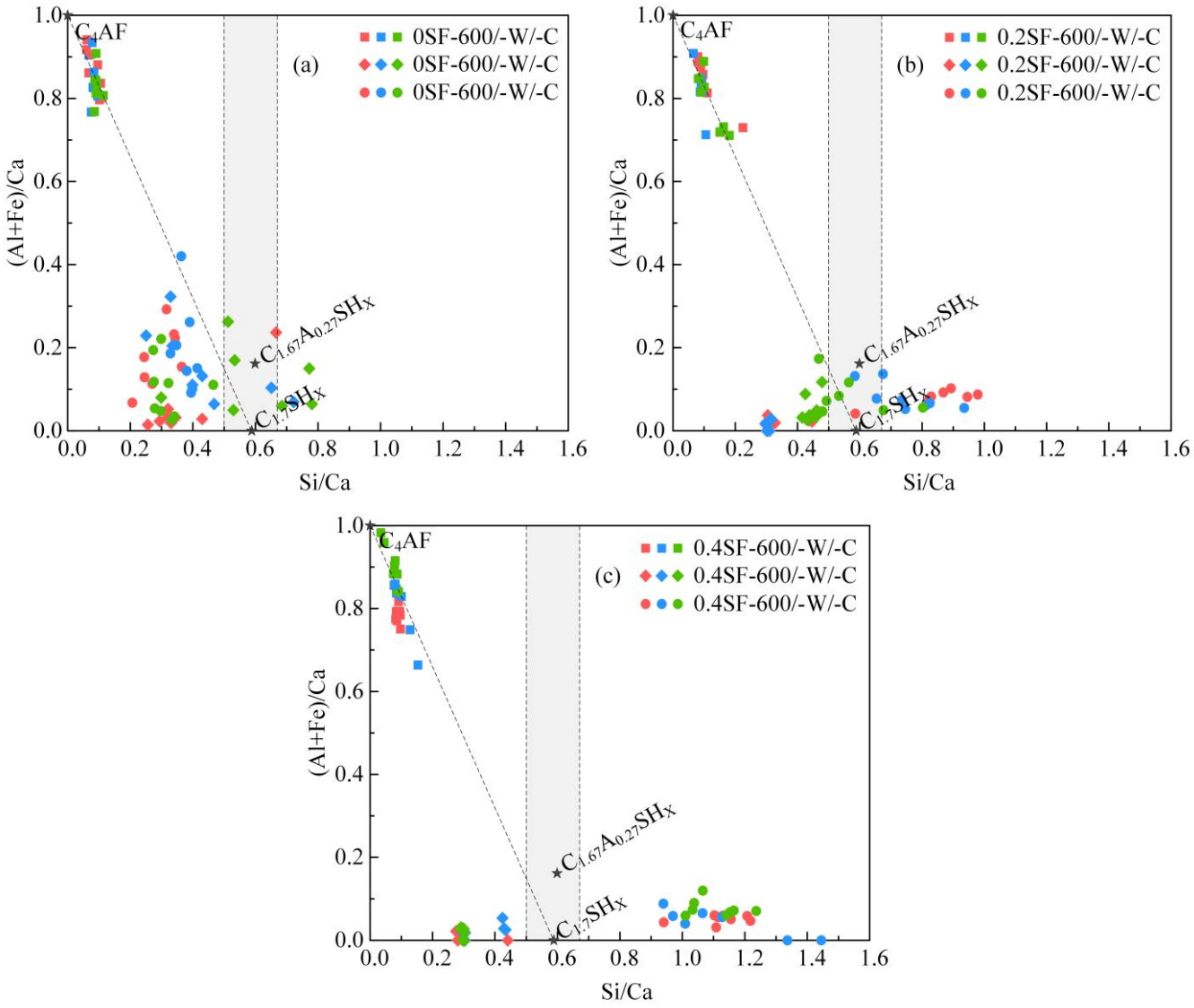

Fig. 17. The molar (Al+Fe)/Ca as a function of the molar Si/Ca of the HPC samples after exposure to a temperature of 600 °C and recuring: (a) 0SF samples; (b) 0.2SF samples; (c) 0.4SF samples.

As shown in Fig. 18, further increasing the temperature to 800 °C does not remarkably change the C_4AF in the three mixtures. For sample 0SF-800, the atomic Si/Ca and (Al+Fe)/Ca in the C_xS_y-cement area remain constant, but the hydration products decompose to form β-C_2S, as evidenced by the XRD results (Fig. 6). On the contrary, noticeable solid-state reactions happen between the unhydrated calcium silicates, hydration products, and residual silica fume in samples 0.2SF-800 and 0.4SF-800. Therefore, no point cluster is observed with an Si/Ca around 0.30 since C_3S reacts with silica to form β-C_2S and γ-C_2S in the

C_xS_y-cement area. In addition, the high silicon-to-calcium ratio in the area of the dehydrated products indicates a new CS phase formed outside the unhydrated cement particles.

After the lime-saturated water recuring, the increase in the Si/Ca in the C_xS_y-cement area is higher in sample 0SF-800-W than in samples 0.2SF-800-W and 0.4SF-800-W, implying a higher dissolution of Ca^{2+} ions, following the XRD results. The rehydration of calcium silicates modifies the Si/Ca in the dehydrated products. The wide variation of Si/Ca of the rehydration products in sample 0SF-800-W from 0.26 to 0.62 indicates the intermixing of C–S–H with microcrystalline CH, while the corresponding Si/Ca of sample 0.2SF-800-W ranges from 0.48 to 0.59, which is in the range of the Si/Ca of C–S–H. On the other hand, CS dominates the dehydration products of sample 0.4SF-800-W, so its Si/Ca does not change significantly due to its low hydration reactivity. Moreover, the stable (Al+Fe)/Ca after rehydration implies the limited precipitation of aluminum-rich rehydration products.

After the water–CO_2 cyclic recuring, C_3S and β-C_2S in the C_xS_y-cement area are carbonated in sample 0SF-800-C, which leads to the leaching of the Ca^{2+} ions into the dehydration products and increases the Si/Ca in the range of 0.44–0.65 via forming $CaCO_3$. Therefore, the Si/Ca in the area of the hydration products ranges from 0.26 to 0.34. The β-C_2S and γ-C_2S of sample 0.2SF-800-C have much lower reactivity, so the Si/Ca remains mainly unchanged in the C_xS_y-cement area. On the other hand, carbonation leads to an Si/Ca in the range of 0.68–0.94 in the dehydration products, corresponding to calcium-modified silica. In sample 0.4SF-800-C, the C_4AF is strongly decalcified as the (Al+Fe)/Ca in this area is as high as 1.2–2.5. The calcium silicates are carbonated, and the Si/Ca increases to a range of 0.54–0.73 in the C_xS_y-cement area. At last, due to the high silica content combined with CS, the Si/Ca of the dehydration products remains very high.

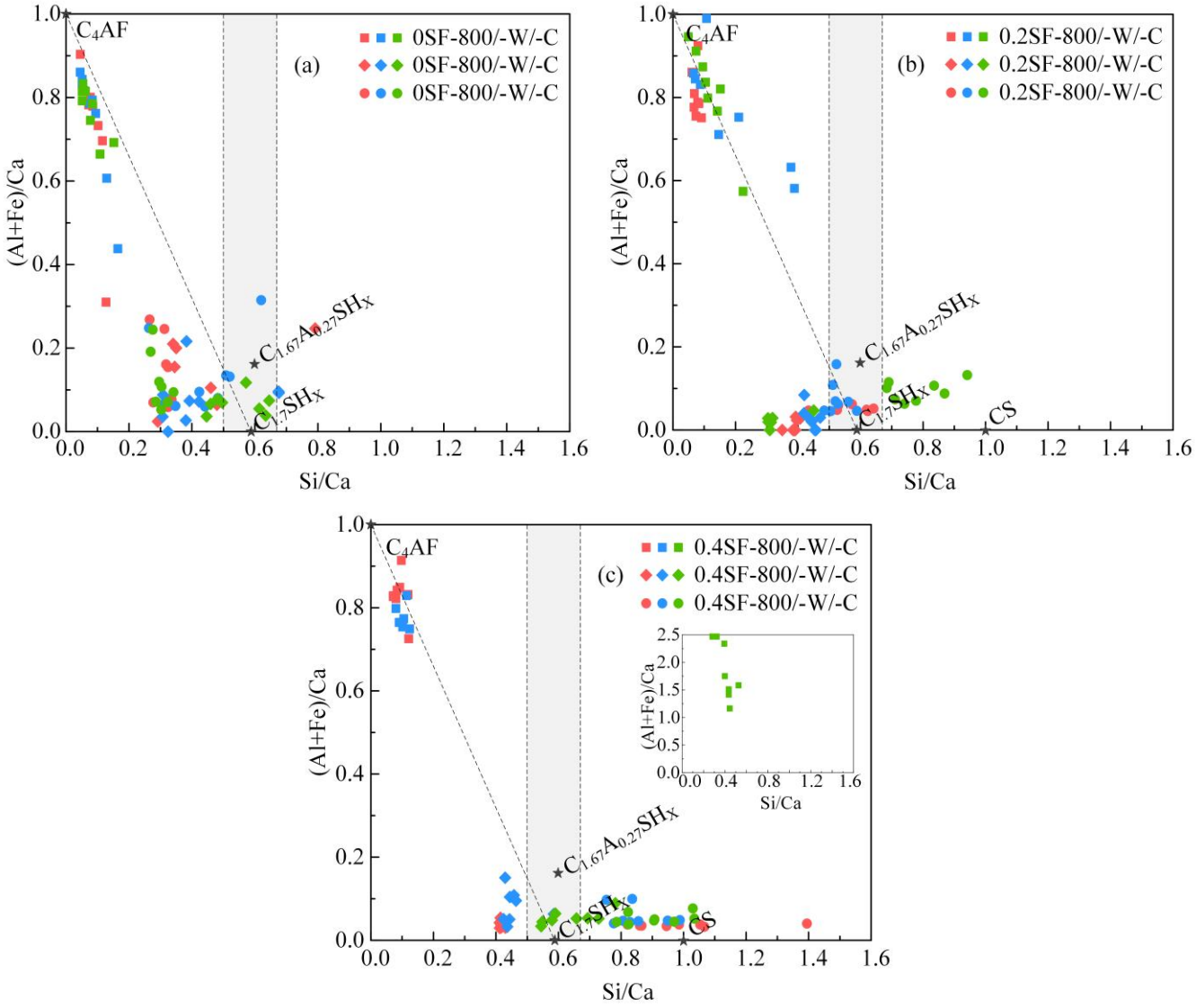

Fig. 18. The molar (Al+Fe)/Ca as a function of the molar Si/Ca of the HPC samples after exposure to a temperature of 800 °C and recuring: (a) 0SF samples; (b) 0.2SF samples; (c) 0.4SF samples.

As mentioned at the beginning of this section, phases in the cement paste are not distinguished after exposing the high-performance concrete specimens to a temperature of 1000 °C. Fig. 19 demonstrates that the Si/Ca of the cement paste of sample 0SF-1000 ranges from 0.35 to 0.44, indicating the presence of C_3S and β-C_2S. A higher Si/Ca of the cement paste of sample 0.2SF-1000 in the range of 0.51–0.77 proves its primary composition of β-C_2S, C_3S_2, and C_2AS. High (Al+Fe)/Ca is seen between points 0.64 and 0.49, indicating an intermixing of C_2AS with calcium silicate phases. Furthermore, sample 0.4SF-1000 is expected to have the highest Si/Ca since CS, C_3S_2, and C_2AS are its main phases. The morphology of the

interfacial transition zone of the sand particles significantly changes as well. The atomic (Al+Fe)/Ca in this area is zero, and the atomic Si/Ca of samples 0SF-1000, 0.2SF-1000, and 0.4SF-1000 is in the range of 0.28–0.52, 0.55–0.73, and 0.88–0.96 respectively, indicating a combination of different calcium silicates.

After the lime-saturated water recuring, both the cement paste and the ITZ are rehydrated. The points in the cement paste of sample 0SF-1000-W exhibit a cluster with an Si/Ca around 0.40, which can be assigned to the unhydrated calcium silicates. The other points in this area show an increased Si/Ca and (Al+Fe)/Ca, implying that they belong to the rehydration products. The considerable variation of (Al+Fe)/Ca indicates the various levels of aluminum binding within this phase. The atomic Si/Ca of the ITZ of sample 0SF-1000-W ranges from 0.41 to 0.58, indicating a combination of microcrystalline CH and C–S–H. In the cement paste of sample 0.2SF-1000-W, the two clusters of points with a Si/Ca of around 0.40 and 0.60 can be identified as β-C_2S and C_3S_2 respectively. The concentrated distribution also shows a low degree of rehydration. Similarly, the cement paste of sample 0.4SF-1000-W is partially hydrated due to the low water reactivity of CS and C_3S_2. The atomic Si/Ca of the interfacial transition zone of sample 0.2SF-1000-W remarkably varies from 0.59 to 1.18, while that of sample 0.4SF-1000-W ranges from 1.06 to 1.53.

After the water–CO_2 cyclic recuring, the C_3S and β-C_2S in the cement paste of sample 0SF-1000-C are carbonated to form calcium carbonates, leading to an Si/Ca between 0.19 and 0.51. In sample 0.2SF-1000-C, β-C_2S is carbonated, and the Si/Ca of the cement paste ranges from 0.20 to 0.52, similar to the Si/Ca of sample 0SF-1000-C. Moreover, CS and C_3S_2 are carbonated in sample 0.4SF-1000-C, and the Si/Ca dramatically varies from 0.42 to 1.38, indicating intermixing of $CaCO_3$ with the silica-rich phase. The interfacial transition zones of the three mixtures are carbonated, and the overall Si/Ca increases in samples

0SF-1000-C, 0.2SF-1000-C, and 0.4SF-1000-C in sequence. The (Al+Fe)/Ca associated with the ITZ of sample 0.4SF-1000-C varies from 0.3 to 0.5, indicating a high level of aluminum binding within this phase.

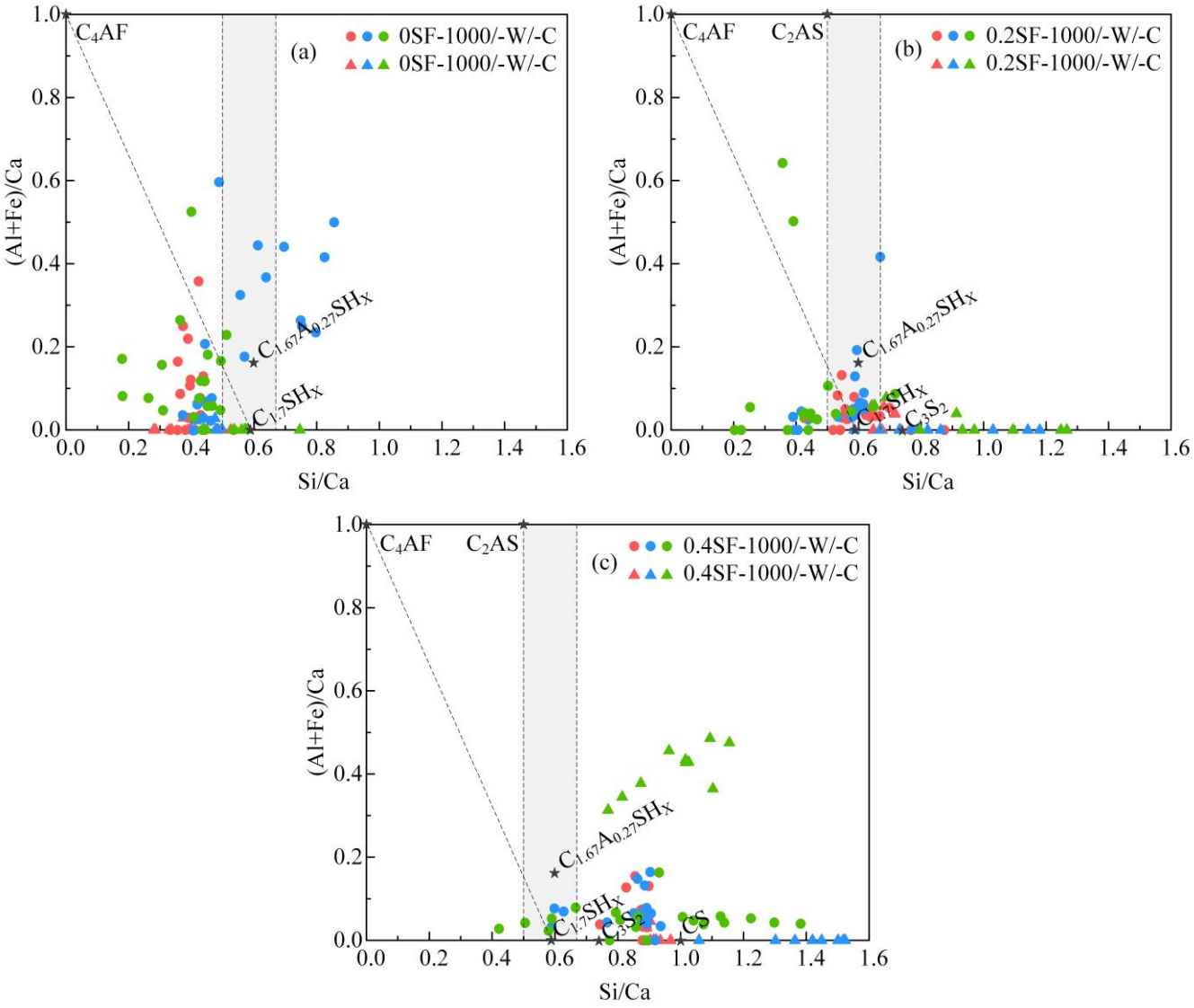

Fig. 19. The molar (Al+Fe)/Ca as a function of the molar Si/Ca of the HPC samples after exposure to a temperature of 1000 °C and recuring: (a) 0SF samples; (b) 0.2SF samples; (c) 0.4SF samples.

3.6. Porosity and pore size distribution

Fig. 20 depicts the pore size distributions of the three samples before heating. The porosity of the HPC samples is divided into three ranges corresponding to microcracks or coarse pores (> 1 μm), large capillaries (50 nm to 1 μm), and small capillaries (6–50 nm), as proposed by previous studies [90-93].

Sample 0SF-25 has the highest porosity of 9.7%, followed by samples 0.2SF-25 and 0.4SF-25 in sequence. Pores in the three samples before heating are mostly smaller than 0.06 µm, indicating a compact microstructure, and the peak pore size of samples 0SF-25 and 0.2SF-25 centers around 0.03 µm. Sample 0.4SF-25 shows an extremely low porosity because of the filling effect of the unreacted silica fume.

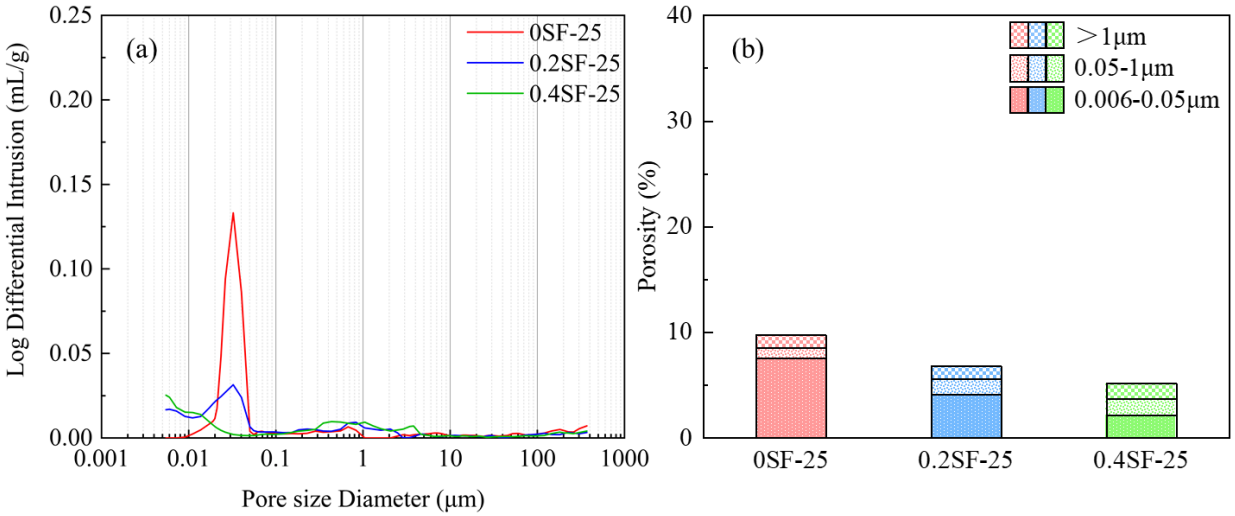

Fig. 20. (a) The pore size distribution of the HPC samples before heating and (b) the porosity of the concrete specimens divided into three ranges.

Fig. 21–Fig. 23 present the porosity of the HPC samples after heating and recuring. According to Fig. 21, exposing samples 0SF-600, 0.2SF-600, and 0.4SF-600 to a temperature of 600 °C increases their porosity to 19.0%, 15.2%, and 9.2% respectively. Their pore size distributions also show a bimodal shape, in which the decomposition of the hydration products creates the left-hand peaks, and the right-hand peaks correspond to the generation of microcracks in samples 0.2SF-600 and 0.4SF-600 [94, 95], agreeing with the SEM observations (see Fig. 12).

After the lime-saturated water recuring, the total porosity of samples 0SF-600, 0.2SF-600, and 0.4SF-600 declines to 10.7%, 4.9%, and 4.1%, respectively, leading to the recovery of the compressive strength of the HPC samples. Fig. 21a demonstrates that 1.6% of the coarse pores and 13.4% of the large capillaries are reduced in sample 0SF-600-W. Due to the filling effects of the rehydration products, the large

capillaries are also segmented and transformed into small ones. Therefore, a shift of the pore size distribution to lower diameters is noted. According to Fig. 21d, all three ranges of pores are reduced in sample 0.2SF-600-W. The decrease in the porosity of sample 0.4SF-600-W mainly occurs in small capillaries because the microcracks are not well filled, as shown in the BSE imaging observations (Fig. 12f). The water–CO_2 cyclic recuring reduces the overall porosity of the three mixtures to a degree slightly higher than that obtained after the lime-saturated water recuring. On the basis of the XRD and BSE imaging results, the reduction in the porosity of the HPC is attributed to the rehydration and carbonation of the C_3S and β-C_2S. The newly formed carbonation products partially fill the coarsened microstructure.

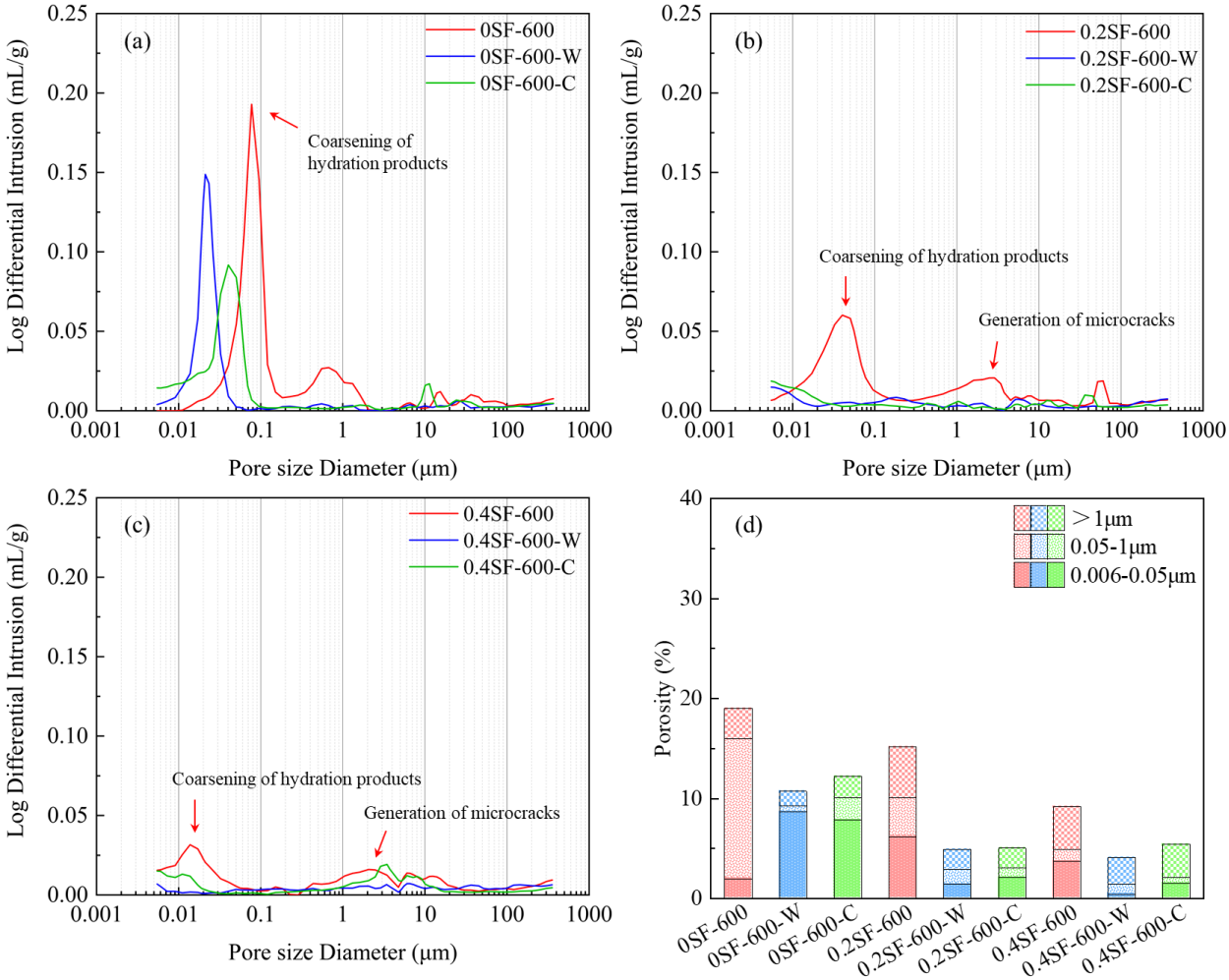

Fig. 21. (a, b, and c) The porosity of the HPC samples after heating at 600 °C and recuring; (d) the porosity of the concrete specimens divided into three ranges.

Exposing the three mixtures to a temperature of 800 °C enlarges their overall porosity to about 25% (see Fig. 22). Moreover, large capillaries, coarse pores, and microcracks dominate the pore structure of the HPC samples. Increasing the silica content reduces the overall porosity of the HPC slightly but increases coarse pores and microcracks larger than 1 μm, agreeing with the SEM observations. The highest fraction of the microcracks explains its drastic strength decrease after exposure to a temperature of 800 °C.

After the lime-saturated water recuring, the microstructure of samples 0SF-800-W and 0.2SF-800-W is refined significantly, and their total porosity declines to a similar level of about 10%. The pore size distribution also shifts to smaller pore diameters. On the contrary, sample 0.4SF-800-W shows the least refinement of its pore structure, and especially, the microcracks are not well healed due to the little rehydration.

After the water–CO_2 cyclic recuring, both the large capillaries and microcracks decrease to a minimal level in samples 0SF-800-C and 0.2SF-800-C; however, although the large capillaries are well healed, the microcracks of sample 0.4SF-800-C are barely reduced, explaining the negligible recovery of the compressive strength of sample 0.4SF-800. It is worth noting that the water–CO_2 cyclic recuring offers an even better overall refinement of the microstructure than the lime-saturated water recuring due to the pore-clogging effects of the carbonation reactions of the rehydration phases [96]. However, the corresponding compressive strength recovery of the HPC by the water–CO_2 cyclic recuring is lower than that by the lime-saturated water recuring, possibly because the compressive strength recovery of the samples correlates closely with large pores.

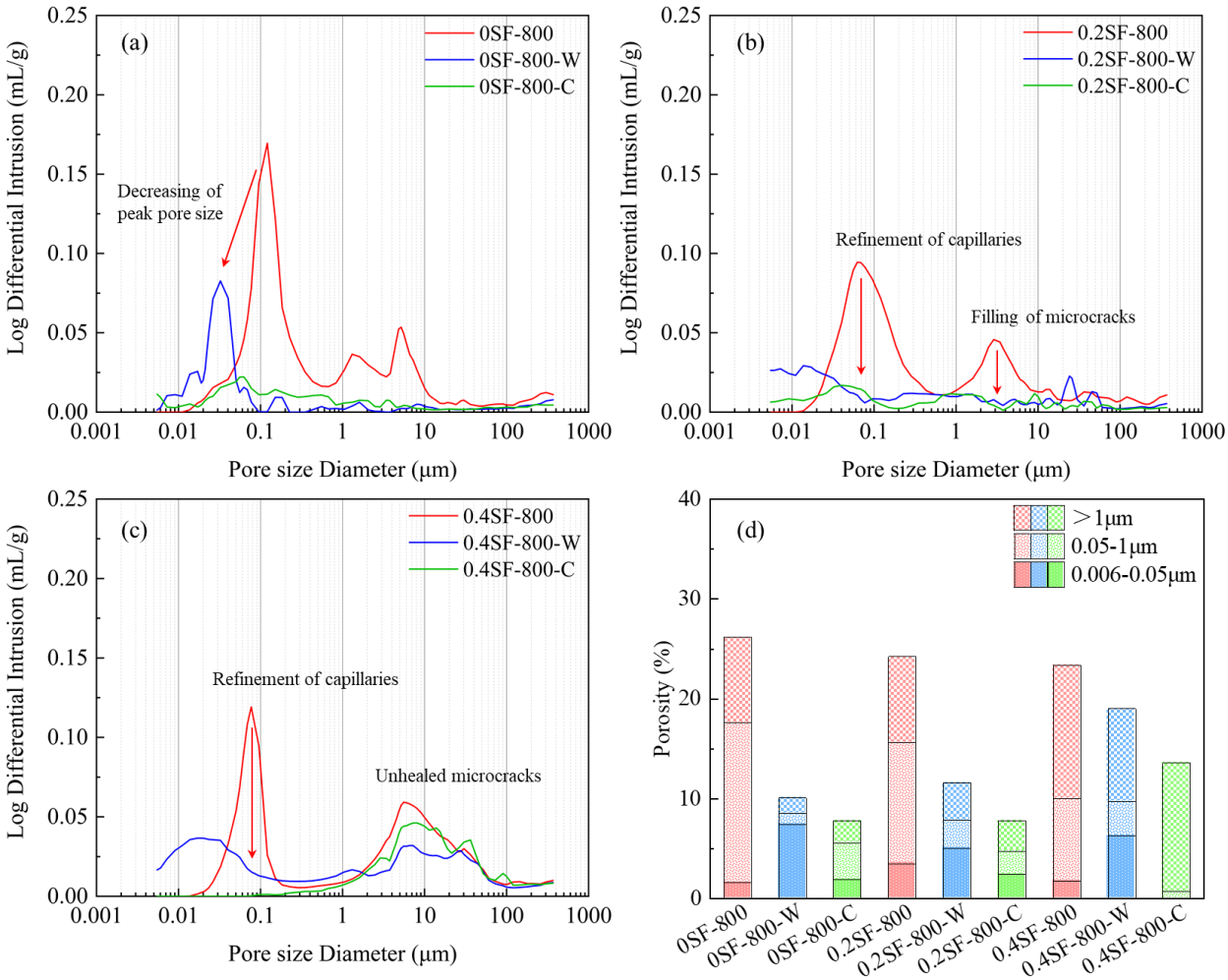

Fig. 22. (a, b, and c) The porosity of the HPC samples after heating at 800 °C and recuring; (d) the porosity of the concrete specimens divided into three ranges.

Heating the high-performance concrete samples at a temperature of 1000 °C severely damages them, and few small capillaries remain in the three mixtures. The total porosity of samples 0SF-1000, 0.2SF-1000, and 0.4SF-1000 increases to 29.9%, 23.4%, and 26.0% respectively. Furthermore, only one main peak with a pore size centered at 0.8 μm can be observed in sample 0SF-1000 (Fig. 23a), following the foam-like microstructure observed by the BSE imaging. Microcracks in sample 0SF-1000 are not obvious compared to samples 0.2SF-1000 and 0.4SF-1000, in which the second peak can be observed in Fig. 23b and c.

After the lime-saturated water recuring, the total porosity of sample 0SF-1000-W declines to 18.4% due to the filling effect of the CH. However, the microstructure of samples 0.2SF-1000-W and 0.4SF-1000-W is barely refined due to the low degree of rehydration (Fig. 23d). On the contrary, the water–CO_2 cyclic recuring refines about half of the porosity of the three mixtures by forming calcium carbonates. Both microcracks and large capillaries are healed in samples 0SF-1000-C and 0.2SF-1000-C. However, only the large capillaries are repaired. The microcracks in sample 0.4SF-1000-C remain unchanged (Fig. 23c), implying that the precipitation of $CaCO_3$ happens in smaller pores of sample 0.4SF-1000-C.

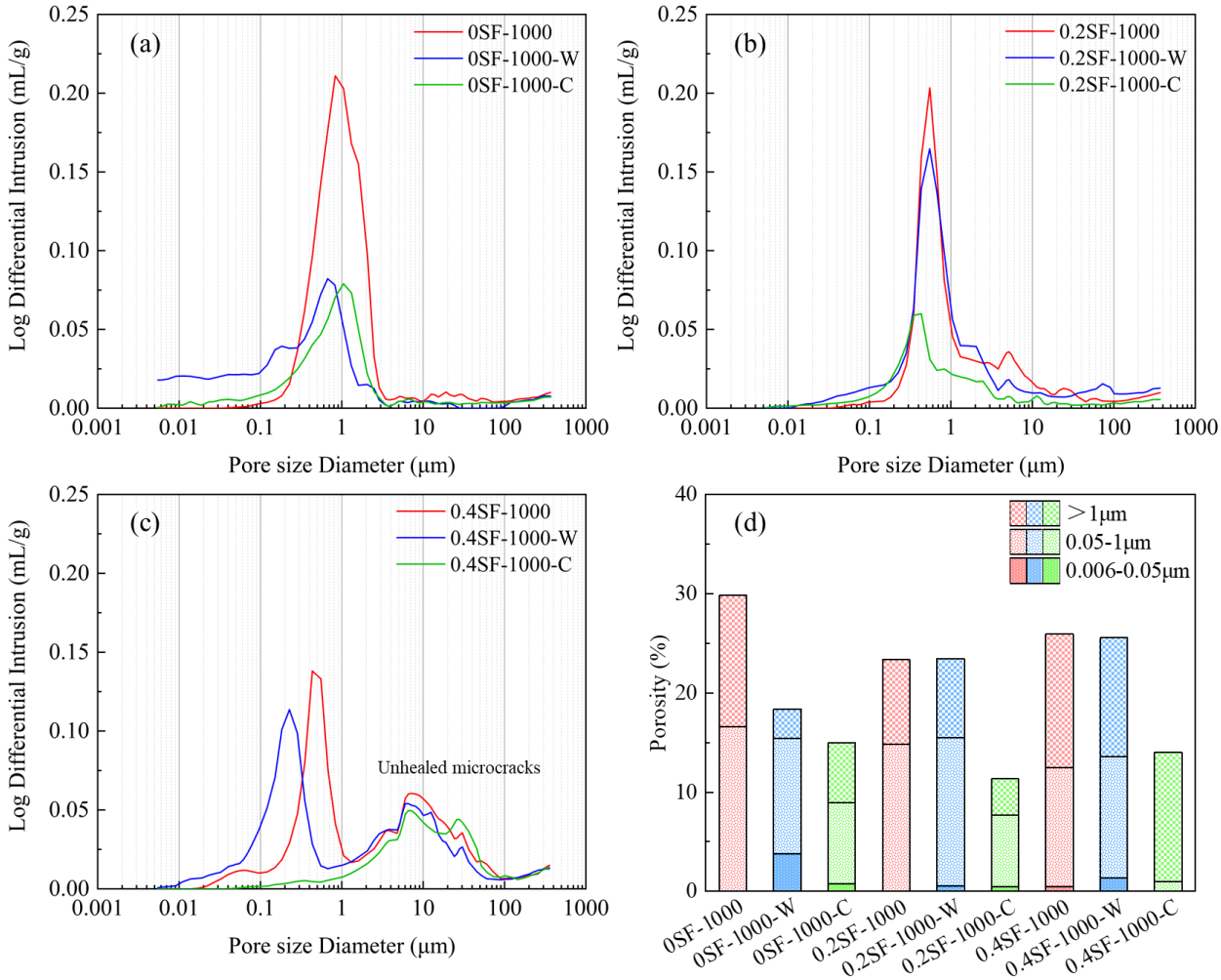

Fig. 23. (a, b, and c) The porosity of the HPC samples after heating at 1000 °C and recuring; (d) the porosity of the concrete specimens divided into three ranges.

Either the reactivity of the dehydration products or the space for the healing products to precipitate is the factor controlling the refinement of the thermally damaged microstructure. If the porosity of the HPC samples after the recuring approaches its original porosity, the reactions are considered restricted by the limited space. Alternatively, the reactivity of the dehydration products retards the recuring reactions. In Fig. 24, the positive porosity values indicate that the thermally damaged pore structure of the HPC specimens is not filled, while the negative values signify an even denser microstructure of the HPC specimens than that of the original samples after recuring. It can be observed that the porosity of all the samples heated at 600 °C, samples 0SF-800-W and 0SF-800-C, and sample 0.2SF-800-C declines remarkably. Their porosity after the recuring approaches or even becomes lower than their original porosity, implying that the limited space restricts the further rehydration and carbonation of the dehydration products. Evidence can be found in the XRD results that a large amount of C_3S and β-C_2S remains after 30 days of recuring. On the other hand, the low amount of C_3S and the low reactivity of other calcium silicate phases hinder the healing of sample 0.2SF-800-W, samples 0.4SF-800-W and 0.4SF-800-C, and the samples heated at 1000 °C. Nevertheless, the water–CO_2 cyclic recuring offers a better healing effect than the lime-saturated water recuring. At last, the compressive strength of samples 0SF-600-W, 0SF-600-C, 0.4SF-600-W, and 0.4SF-600-C exceeds their original compressive strength before heating. However, the microstructure formed by the healing products is not as dense as that of the original samples, indicating that except for compactness, the morphology, interlocking of crystals, and binding property of the microstructure of recured HPC contribute to its compressive strength.

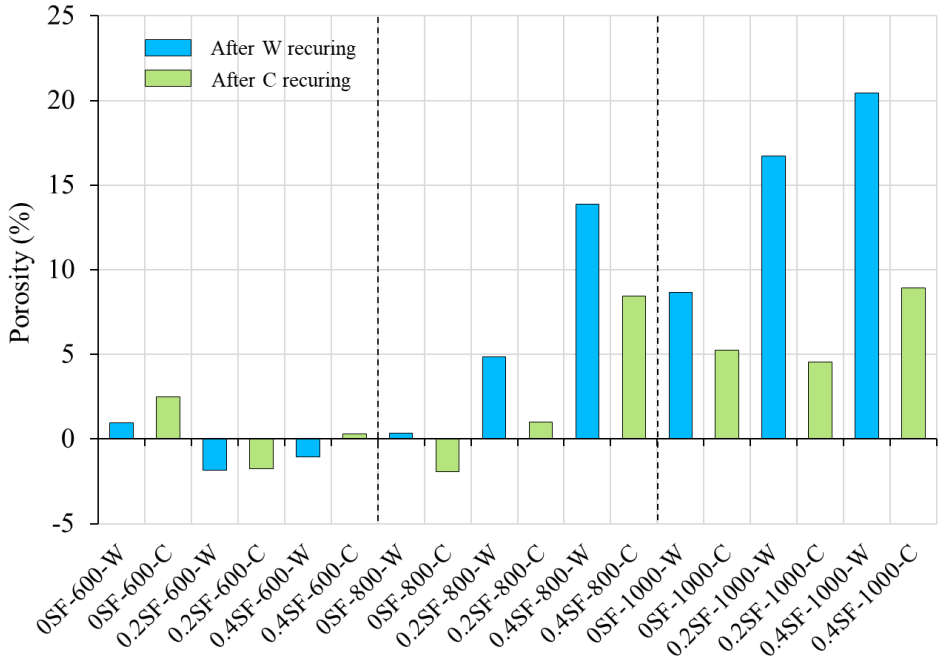

Fig. 24. Comparing the porosity of HPC specimens after recuring with their corresponding original porosity.

4. Summary and schematic illustration

4.1. Summary of characterizations

Table 4 summarizes the changes in the high-performance concrete samples in terms of the compressive strength, phase assemblage, and microstructure after heating and recuring based on the results of multiple characterizations. The compressive strength of the HPC samples increases after heating at 400 °C but starts to decrease after heating at 600, 800, and 1000 °C.

After exposing the HPC specimens to a temperature of 600 °C, a large quantity of unhydrated C_3S and β-C_2S remains, while the microcracks generated in samples 0.2SF-600 and 0.4SF-600 coarsen the microstructure. CH and C–S–H are the major rehydration products, and calcium carbonates and silica gel form after the carbonation to densify the coarsened cement paste and fill the microcracks of the thermally damaged HPC samples. As a result, the lime-saturated water and water–CO_2 cyclic recuring offer significant compressive strength recovery for the three concrete mixtures.

The thermal damage to the concrete microstructure intensifies after heating the HPC specimens at 800 °C, remarkably increasing their overall porosity. C_3S remains in sample 0SF-800, but solid-state reactions happen between C_3S and silica to form γ-C_2S and CS in samples 0.2SF-800 and 0.4SF-800. After recuring, samples 0SF-800-W and 0SF-800-C present the highest strength recovery due to the newly formed CH, C–S–H, and $CaCO_3$ polymorphs refining the pore structure of the cement paste. The compressive strength recovery of samples 0.2SF-800-W and 0.2SF-800-C is lower due to the absence of C_3S, and sample 0.4SF-800 shows negligible compressive strength recovery because the microcracks are not effectively healed due to the limited reactions of the γ-C_2S and CS.

After exposing the samples to a temperature of 1000 °C, the cement paste exhibits a foam-like structure with disintegrated cement grains and merged hydration products, and microcracks in samples 0.2SF-1000 and 0.4SF-1000 are enlarged. C_3S and β-C_2S dominate more than 90% of the phases in sample 0SF-1000, while C_3S_2 and C_2AS form in samples 0.2SF-1000 and 0.4SF-1000. Low-water reactivity phases dominate more than 80% of the total weight of sample 0.4SF-1000. After the lime-saturated water recuring, only sample 0SF-1000 is effectively rehydrated, but its microstructure is still porous and poorly cohesive. The water–CO_2 cyclic recuring coalesces the cement paste and partially fills the microcracks by forming calcium carbonates with different degrees of crystallinity. As a result, only the water–CO_2 cyclic recuring impacts the compressive strength recovery of high-performance concrete.

Table 4. The change in the HPC samples after heating and recuring.

Specimen	0SF	0.2SF	0.4SF
600	Decrease of strength, decomposition of $Ca(OH)_2$, and coarsening of matrix	Decrease of strength, decomposition of $Ca(OH)_2$, Coarsening of matrix with microcracks	Slight increase of strength, decomposition of $Ca(OH)_2$, Coarsening of matrix with microcracks
600-W	Significant strength recovery with densification of matrix by $Ca(OH)_2$ and amorphous phases	Significant strength recovery with densification of matrix by amorphous phases and filling of microcracks by AFt	Significant strength recovery with densification of matrix by amorphous phases and narrowed microcracks
600-C	Significant strength recovery with densification of matrix by $CaCO_3$	Significant strength recovery with densification of matrix and filling of microcracks by $CaCO_3$	Significant strength recovery with densification of matrix and filling of microcracks by $CaCO_3$

800	Significant decrease of strength with coarsened matrix and enlarged pores	Significant decrease of strength, formation of CS, coarsening of matrix and microcracks	Significant decrease of strength, formation of CS, coarsening of matrix and microcracks
800-W	Significant strength recovery with densification of matrix by $Ca(OH)_2$ and amorphous phases	Significant strength recovery with densification of matrix by amorphous phases and filling of microcracks by AFt	No notable change
800-C	Lower strength recovery than lime-saturated water recuring with densification of matrix by $CaCO_3$ and amorphous phases	Comparable strength recovery with lime-saturated water recuring with densification of matrix and filling of cracks by $CaCO_3$ and amorphous phases	No strength recovery, densification of matrix by $CaCO_3$ but unfilled microcracks
1000	Further decrease of strength with foam-like matrix and crystalline ITZ	Further decrease of strength, formation of low lime phases, coarsening of matrix with microcracks	Similar strength with that of the 800-C sample caused by coarsened matrix and microcracks
1000-W	Slight strength recovery with densification of matrix by $Ca(OH)_2$ and amorphous phases	Almost no strength recovery with slight densification of matrix by amorphous phases	No notable change
1000-C	Significant strength recovery with densification of matrix by $CaCO_3$ and amorphous phases	Significant strength recovery with densification of matrix and filling of microcracks by $CaCO_3$	Slight strength recovery with densification of matrix by $CaCO_3$ and amorphous phases

4.2. Hydration and carbonation processes

To illustrate the mechanisms for the recovery of the compressive strength of HPC, we illustrate a schematic of the hydration and carbonation processes in Fig. 25, focusing on the processes leading to the filling of the microcracks and the densification of the cement paste matrix. Water has proved to be essential for recuring; in fact, it is necessary for dissolving the remained cement and dehydrated products and acts as a transport medium. When the lime-saturated water permeates the thermally damaged HPC samples, Ca^{2+} and OH^- ions diffuse from the microcracks into the bulk cement paste. Meanwhile, the leaching of ions from the dehydrated products and the remaining cement particles initiates supersaturation of the pore solution. Therefore, the rehydration products start to precipitate in the porous cement paste. Generally, nucleation is categorized into “homogenous nucleation” and “heterogeneous nucleation”. Compared to homogenous nucleation, which happens under supersaturation conditions spontaneously [97], heterogeneous nucleation occurs at specific preferential sites with a lower free energy barrier [98]. In the present study, the skeleton of the thermally damaged bulk cement paste is the ideal preferential site,

facilitating the heterogeneous nucleation of the rehydration products and accelerating the healing rate. The saturation criterion of products with lower solubility such as C–S–H is more easily reached [99], so C–S–H mainly precipitates in the bulk cement paste. Ions such as $H_2SiO_4^{2-}$, $Al(OH)_4^-$, and SO_4^{2-} can leach from the bulk cement paste into microcracks due to the concentration gradient, giving rise to the deposition of AFt in the microcracks. At last, CH precipitates in both the bulk cement paste and the microcracks.

This analysis agrees with the observation that CH and C–S–H precipitate inside the thermally damaged cement paste of 0SF samples. CH is consumed in pozzolanic reaction with the silicate phase in the cement paste to form C–S–H in 0.2SF samples, and AFt can be observed in the microcracks. The degree of reaction of 0.4SF samples is minimal due to the low hydration reactivity of the dehydrated products.

The cycling of hydration and carbonation increases complexity during the water–CO_2 cyclic recuring. The diffusivity of CO_2 is four orders of magnitudes lower in water than in the air [29], so the carbonation rate of the unsaturated concrete is much higher than that of the saturated concrete. Specifically, the carbonation of hydration products evolves much faster in an atmosphere with a relative humidity between 50% and 70% [100, 101]. In the carbonation stage, low relative humidity of 40% promotes drying of the saturated samples, and the microcracks dry before the bulk cement paste because of their larger pore dimensions and lower capillary force. Moreover, the permeation of CO_2 into the microcracks leads to the precipitation of $CaCO_3$ and the carbonation of CH. Therefore, $CaCO_3$ polymorphs fill the microcracks in samples 0.2SF-600-C, 0.2SF-800-C, 0.2SF-1000-C, and 0.4SF-600-C, as evidenced by the SEM results. However, microcracks in samples 0.4SF-800-C and 0.4SF-1000-C are not well healed due to the low reactivity of the dehydration products. It is worth noting that the $CaCO_3$ precipitated merely depends on the Ca^{2+} ions supplied by the lime-saturated water is far from enough to fill the coarsened pore structure of HPC, indicating the transfer of mobile Ca^{2+} ions from the dissolution of the dehydrated products and unhydrated

cement particles outward toward the microcracks. This explains the higher degree of reaction of the dehydrated products after water–CO_2 cyclic recuring than the lime-saturated water recuring.

When CO_2 further permeates into the cement paste of HPC, the initially formed rehydration products and the unhydrated calcium silicates start to be carbonated to form various polymorphs of $CaCO_3$, silica gel, and aluminum gel in the cement paste [44, 45, 102]. The water molecules released from the carbonation of the hydrates support this continuing hydration, and the depletion of Ca^{2+} ions leads to the decalcification of the existing CH, C–S–H, and AFt, which reduces the volume inside the microstructure of the samples [103]. However, the $CaCO_3$ crystals can precipitate and grow in the voids, giving rise to an 11%–12% expansion, compensating for the shrinkage [104, 105]. $CaCO_3$ crystals have excellent resistance to cracking because of their interaction with the surrounding microstructure by ionic and covalent bonds [106]. Therefore, the $CaCO_3$ crystals intermix with the modified C–S–H and silica gel to form a cohesive nanogranular matrix, which increases the packing density and bonding of the thermally damaged cement paste [63]. Finally, the newly formed $CaCO_3$ layer on the surface of the CH crystals may obstruct the diffusion of Ca^{2+} ions and CO_2, inhibiting further carbonation [103, 107-109]. However, the CH is fully consumed owning to the water–CO_2 cyclic recuring in this study.

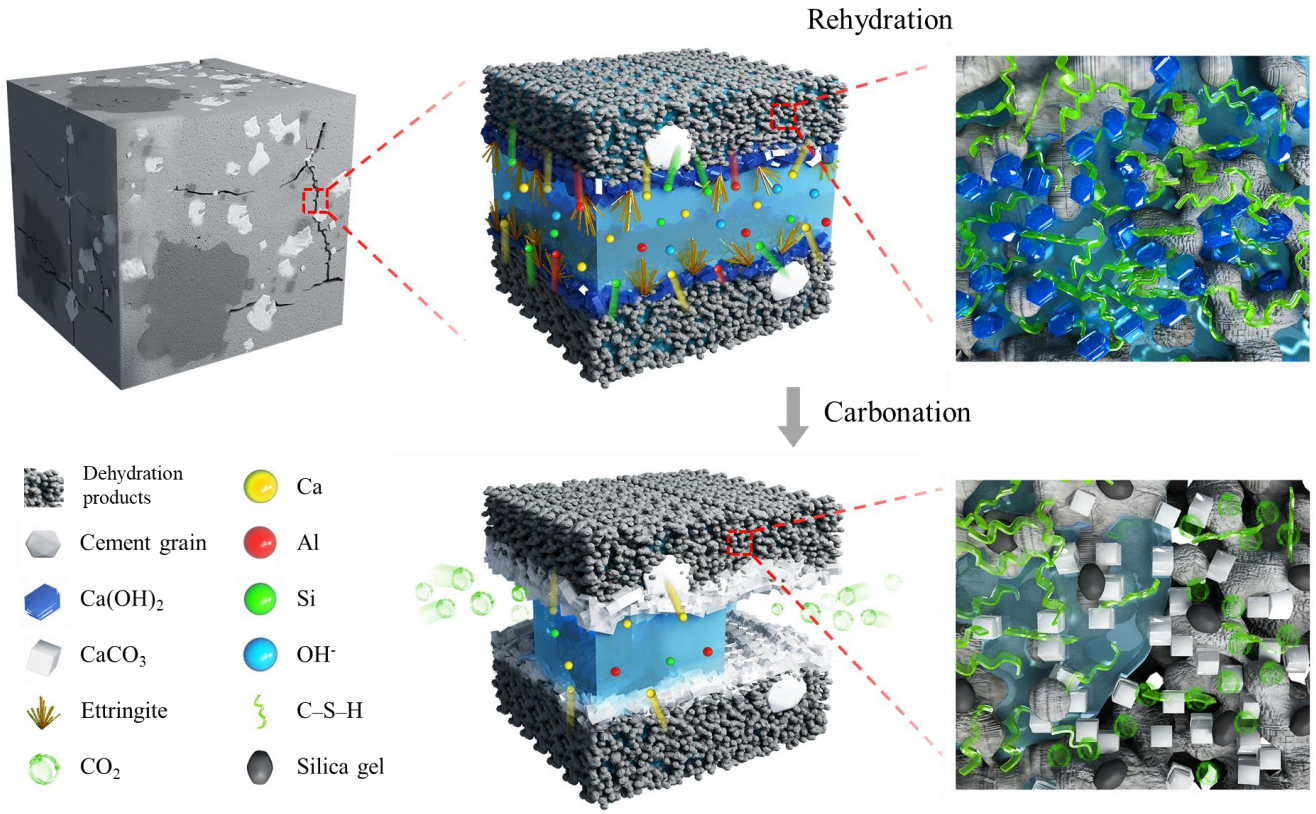

Fig. 25. A schematic of the hydration and carbonation processes.

5. Conclusions

This work studied the effects of two recuring regimes, namely lime-saturated water recuring and water–CO_2 cyclic recuring, on the compressive strength recovery of thermally damaged HPC with three different silica fume contents. Multiple characterization methods, including XRD, TGA, SEM, MIP, and EDX, quantitatively characterized the phase assemblage, microstructure, porosity, and elemental distribution of the HPC samples before heating, after heating, and after recuring. The results provide insight into the evolving microstructure of HPC and shed light on the mechanisms for the compressive strength recovery of HPC.

C_3S and β-C_2S in the unhydrated cement remained in all the mixtures exposed to a temperature of 600 °C. However, for 0.2SF and 0.4SF samples, the C_3S and β-C_2S reacted with silicate to form low-calcium phase γ-C_2S and CS at 800 °C and generated C_3S_2, CS, and C_2AS after the samples were exposed to 1000 °C.

The decomposition and phase transformation of hydration products led to the coarsening of the cement paste matrix and the generation of microcracks.

The recovery of the compressive strength of HPC primarily depends on the healing of microcracks and larger pores, followed by the filling of large capillaries. Lime-saturated water recuring offered slightly higher strength recovery than water–CO_2 cyclic recuring for all the mixtures exposed to 600 °C and for 0SF and 0.2SF samples exposed to 800 °C. The recovered compressive strength even exceeded the original compressive strength before heating due to the formation of CH and C–S–H after rehydration and the generation of calcium carbonates and silica-rich phase after carbonation. After 1000 °C exposure, only water–CO_2 cyclic recuring recovered the compressive strength because the dehydrated phases had low water reactivity, while the formation of the carbonation products coalesced the cement paste and partially filled the microcracks of the HPC specimens. Finally, the test results were summarized, and schematic diagrams were plotted to provide a thorough understanding of the healing process of the thermally damaged microstructure of HPC.

Declaration of competing interest

The authors declare that they have no known competing financial interests or personal relationships that could have appeared to influence the work reported in this paper.

Acknowledgments

This work was supported by the National Science Fund for Distinguished Young Scholars [grant number 52025081], the National Natural Science Foundation of China [grant number 52008136], and the Shenzhen Science and Technology Program [grant number GXWD20201230155427003-20200823110420001].

References

[1] H.J. Yim, J.H. Kim, S.-J. Park, H.-G. Kwak, Characterization of thermally damaged concrete using a nonlinear ultrasonic method, Cem. Concr. Res., 42 (2012) 1438-1446.
[2] Z.P. Bažant, M.F. Kaplan, Z.P. Bazant, Concrete at high temperatures: material properties and mathematical models, (1996).
[3] A. Tovey, Assessment and repair of fire-damaged concrete structures-an update, Spec. Publ., 92 (1986) 47-62.
[4] E. Denarié, E. Brühwiler, Structural rehabilitations with ultra high performance fibre reinforced concretes, Restor. build. monum., 12 (2006) 453-465.
[5] A.H. Akca, N. Özyurt, Effects of re-curing on residual mechanical properties of concrete after high temperature exposure, Constr. Build. Mater., 159 (2018) 540-552.
[6] W.-M. Lin, T. Lin, L. Powers-Couche, Microstructures of fire-damaged concrete, ACI Mater. J. , 93 (1996) 199-205.
[7] C.-S. Poon, S. Azhar, M. Anson, Y.-L. Wong, Strength and durability recovery of fire-damaged concrete after post-fire-curing, Cem. Concr. Res., 31 (2001) 1307-1318.
[8] G. Khoury, Compressive strength of concrete at high temperatures: a reassessment, Mag. Concr. Res., 44 (1992) 291-309.
[9] H.J. Yim, S.-J. Park, Y. Jun, Physicochemical and mechanical changes of thermally damaged cement pastes and concrete for re-curing conditions, Cem. Concr. Res., 125 (2019) 105831.
[10] L. Li, P. Jia, J. Dong, L. Shi, G. Zhang, Q. Wang, Effects of cement dosage and cooling regimes on the compressive strength of concrete after post-fire-curing from 800 °C, Constr. Build. Mater., 142 (2017) 208-220.
[11] A.H. Akca, N. Özyurt, Effects of re-curing on microstructure of concrete after high temperature exposure, Constr. Build. Mater., 168 (2018) 431-441.
[12] S.-J. Park, H.J. Yim, H.-G. Kwak, Effects of post-fire curing conditions on the restoration of material properties of fire-damaged concrete, Constr. Build. Mater., 99 (2015) 90-98.
[13] M. Henry, I.S. Darma, T. Sugiyama, Analysis of the effect of heating and re-curing on the microstructure of high-strength concrete using X-ray CT, Constr. Build. Mater., 67 (2014) 37-46.
[14] H.J. Yim, S.-J. Park, Y. Jun, Physicochemical and mechanical changes of thermally damaged cement pastes and concrete for re-curing conditions, Cem. Concr. Res., 125 (2019).
[15] A. Rahim, U.K. Sharma, K. Murugesan, A. Sharma, P. Arora, Multi-response optimization of post-fire residual compressive strength of high performance concrete, Constr. Build. Mater., 38 (2013) 265-273.
[16] Q. Ma, R. Guo, Z. Zhao, Z. Lin, K. He, Mechanical properties of concrete at high temperature—A review, Constr. Build. Mater., 93 (2015) 371-383.
[17] B. Jeyaprabha, G. Elangovan, P. Prakash, Effects of elevated temperature and water quenching on strength and microstructure of mortars with river sand substitutes, Constr. Build. Mater., 114 (2016) 688-698.
[18] D. Wang, C. Shi, Z. Wu, J. Xiao, Z. Huang, Z. Fang, A review on ultra high performance concrete: Part II. Hydration, microstructure and properties, Constr. Build. Mater., 96 (2015) 368-377.
[19] K.H. Khayat, W. Meng, K. Vallurupalli, L. Teng, Rheological properties of ultra-high-performance concrete—An overview, Cem. Concr. Res., 124 (2019) 105828.
[20] R. Yu, P. Spiesz, H.J.H. Brouwers, Mix design and properties assessment of Ultra-High Performance Fibre Reinforced Concrete (UHPFRC), Cem. Concr. Res., 56 (2014) 29-39.
[21] Y. Li, Y. Zhang, E.-H. Yang, K.H. Tan, Effects of geometry and fraction of polypropylene fibers on permeability of ultra-high performance concrete after heat exposure, Cem. Concr. Res., 116 (2019) 168-178.
[22] Y. Li, K.H. Tan, E.-H. Yang, Influence of aggregate size and inclusion of polypropylene and steel fibers on the hot permeability of ultra-high performance concrete (UHPC) at elevated temperature, Constr. Build. Mater., 169 (2018) 629-637.
[23] W. Ashraf, J. Olek, J. Jain, Microscopic features of non-hydraulic calcium silicate cement paste and mortar, Cem. Concr. Res., 100 (2017) 361-372.
[24] D. Wang, Y. Fang, Y. Zhang, J. Chang, Changes in mineral composition, growth of calcite crystal, and promotion of physico-chemical properties induced by carbonation of β-C_2S, J. CO_2 Util., 34 (2019) 149-162.

[25] W. Ashraf, J. Olek, Carbonation behavior of hydraulic and non-hydraulic calcium silicates: potential of utilizing low-lime calcium silicates in cement-based materials, J. Mater. Sci., 51 (2016) 6173-6191.
[26] J. Bukowski, R.L. Berger, Reactivity and strength development of CO_2 activated non-hydraulic calcium silicates, Cem. Concr. Res., 9 (1979) 57-68.
[27] J.G. Jang, H.K. Lee, Microstructural densification and CO_2 uptake promoted by the carbonation curing of belite-rich Portland cement, Cem. Concr. Res., 82 (2016) 50-57.
[28] Z. Liu, W. Meng, Fundamental understanding of carbonation curing and durability of carbonation-cured cement-based composites: A review, J. CO_2 Util., 44 (2021).
[29] V.G. Papadakis, C.G. Vayenas, M. Fardis, A reaction engineering approach to the problem of concrete carbonation, AIChE J., 35 (1989) 1639-1650.
[30] M. Fernandez Bertos, S.J. Simons, C.D. Hills, P.J. Carey, A review of accelerated carbonation technology in the treatment of cement-based materials and sequestration of CO_2, J. Hazard. Mater., 112 (2004) 193-205.
[31] A.S.T. Mater., ASTM C 109/C 109 M-11, Standard Test Method for Compressive Strength of Hydraulic Cement Mortars (Using 2-in. or 50-mm Cube Specimens), 2011.
[32] I. Odler, Hydration, setting and hardening of Portland cement, Lea's chemistry of cement and concrete, (1998).
[33] H. Fares, S. Remond, A. Noumowe, A. Cousture, High temperature behaviour of self-consolidating concrete, Cem. Concr. Res., 40 (2010) 488-496.
[34] Y. Li, E.-H. Yang, K.H. Tan, Effects of heating followed by water quenching on strength and microstructure of ultra-high performance concrete, Constr. Build. Mater., 207 (2019) 403-411.
[35] H. Yazıcı, E. Deniz, B. Baradan, The effect of autoclave pressure, temperature and duration time on mechanical properties of reactive powder concrete, Constr. Build. Mater., 42 (2013) 53-63.
[36] C.-S. Poon, S. Azhar, M. Anson, Y.-L. Wong, Comparison of the strength and durability performance of normal-and high-strength pozzolanic concretes at elevated temperatures, Cem. Concr. Res., 31 (2001) 1291-1300.
[37] Q. Zhang, G. Ye, E. Koenders, Investigation of the structure of heated Portland cement paste by using various techniques, Constr. Build. Mater., 38 (2013) 1040-1050.
[38] L. Li, L. Shi, Q. Wang, Y. Liu, J. Dong, H. Zhang, G. Zhang, A review on the recovery of fire-damaged concrete with post-fire-curing, Constr. Build. Mater., 237 (2020).
[39] X. Ming, M. Cao, X. Lv, H. Yin, L. Li, Z. Liu, Effects of high temperature and post-fire-curing on compressive strength and microstructure of calcium carbonate whisker-fly ash-cement system, Constr. Build. Mater., 244 (2020).
[40] Q. Zhou, F.P. Glasser, Thermal stability and decomposition mechanisms of ettringite at< 120 °C, Cem. Concr. Res., 31 (2001) 1333-1339.
[41] E. Stepkowska, J. Blanes, F. Franco, C. Real, J. Pérez-Rodrıguez, Phase transformation on heating of an aged cement paste, Thermochim. Acta, 420 (2004) 79-87.
[42] M. Tantawy, Effect of high temperatures on the microstructure of cement paste, J. Mater. Sci. Chem. Eng., 5 (2017) 33.
[43] D. Wang, J. Chang, Comparison on accelerated carbonation of β-C_2S, $Ca(OH)_2$, and C_4AF: Reaction degree, multi-properties, and products, Constr. Build. Mater., 224 (2019) 336-347.
[44] A.E. Morandeau, C.E. White, In situ X-ray pair distribution function analysis of accelerated carbonation of a synthetic calcium–silicate–hydrate gel, J. Mater. Chem. A, 3 (2015) 8597-8605.
[45] A. Morandeau, M. Thiéry, P. Dangla, Investigation of the carbonation mechanism of CH and C-S-H in terms of kinetics, microstructure changes and moisture properties, Cem. Concr. Res., 56 (2014) 153-170.
[46] M. Saillio, V. Baroghel-Bouny, S. Pradelle, M. Bertin, J. Vincent, J.-B. d'Espinose de Lacaillerie, Effect of supplementary cementitious materials on carbonation of cement pastes, Cem. Concr. Res., 142 (2021).
[47] Y. Li, W. Liu, F. Xing, S. Wang, L. Tang, S. Lin, Z. Dong, Carbonation of the synthetic calcium silicate hydrate (C-S-H) under different concentrations of CO_2: Chemical phases analysis and kinetics, J. CO_2 Util., 35 (2020) 303-313.
[48] P.H. Borges, J.O. Costa, N.B. Milestone, C.J. Lynsdale, R.E. Streatfield, Carbonation of CH and C–S–H in composite cement pastes containing high amounts of BFS, Cem. Concr. Res., 40 (2010) 284-292.
[49] M. Castellote, L. Fernandez, C. Andrade, C. Alonso, Chemical changes and phase analysis of OPC pastes carbonated at different CO_2 concentrations, Materials and Structures, 42 (2008) 515-525.

[50] R. Serpell, F. Zunino, Recycling of hydrated cement pastes by synthesis of α′H-C_2S, Cem. Concr. Res., 100 (2017) 398-412.
[51] R. Serpell, M. Lopez, Properties of mortars produced with reactivated cementitious materials, Cem. Concr. Compos., 64 (2015) 16-26.
[52] P. Hewlett, M. Liska, Lea's chemistry of cement and concrete, Butterworth-Heinemann2019.
[53] W. Ashraf, J. Olek, Elucidating the accelerated carbonation products of calcium silicates using multi-technique approach, J. CO_2 Util., 23 (2018) 61-74.
[54] P. Worsfold, A. Townshend, C.F. Poole, M. Miró, Encyclopedia of analytical science, Elsevier2019.
[55] Y. Zhao, L. Lu, S. Wang, C. Gong, Y. Huang, Modification of dicalcium silicates phase composition by BaO, SO_3 and MgO, J. Inorg. Organomet. Polym. Mater., 23 (2013) 930-936.
[56] K. Morsli, G. Angeles, M. Zahir, M.A. Aranda, Mineralogical phase analysis of alkali and sulfate bearing belite rich laboratory clinkers, Cem. Concr. Res., 37 (2007) 639-646.
[57] L. Nicoleau, A. Nonat, A new view on the kinetics of tricalcium silicate hydration, Cem. Concr. Res., 86 (2016) 1-11.
[58] P. Juilland, E. Gallucci, R. Flatt, K. Scrivener, Dissolution theory applied to the induction period in alite hydration, Cem. Concr. Res., 40 (2010) 831-844.
[59] W. Cole, B. Kroone, Carbon dioxide in hydrated Portland cement, Journal Proceedings, 1960, pp. 1275-1296.
[60] C.Y. Tai, P.C. Chen, Nucleation, agglomeration and crystal morphology of calcium carbonate, AIChE J., 41 (1995) 68-77.
[61] M. Thiery, G. Villain, P. Dangla, G. Platret, Investigation of the carbonation front shape on cementitious materials: Effects of the chemical kinetics, Cem. Concr. Res., 37 (2007) 1047-1058.
[62] L. Fernández-Carrasco, D. Torréns-Martín, S. Martínez-Ramírez, Carbonation of ternary building cementing materials, Cem. Concr. Compos., 34 (2012) 1180-1186.
[63] B.J. Zhan, D.X. Xuan, C.S. Poon, K.L. Scrivener, Multi-scale investigation on mechanical behavior and microstructural alteration of C-S-H in carbonated Alite paste, Cem. Concr. Res., 144 (2021).
[64] T.F. Sevelsted, J. Skibsted, Carbonation of C–S–H and C–A–S–H samples studied by ^{13}C, ^{27}Al and ^{29}Si MAS NMR spectroscopy, Cem. Concr. Res., 71 (2015) 56-65.
[65] V. Shah, K. Scrivener, B. Bhattacharjee, S. Bishnoi, Changes in microstructure characteristics of cement paste on carbonation, Cem. Concr. Res., 109 (2018) 184-197.
[66] B.J. Zhan, D.X. Xuan, C.S. Poon, C.J. Shi, Mechanism for rapid hardening of cement pastes under coupled CO2-water curing regime, Cem. Concr. Compos., 97 (2019) 78-88.
[67] M. Liu, S. Hong, Y. Wang, J. Zhang, D. Hou, B. Dong, Compositions and microstructures of hardened cement paste with carbonation curing and further water curing, Constr. Build. Mater., 267 (2021) 121724.
[68] T. Chen, X. Gao, Effect of carbonation curing regime on strength and microstructure of Portland cement paste, J. CO_2 Util., 34 (2019) 74-86.
[69] Z. Shi, B. Lothenbach, M.R. Geiker, J. Kaufmann, A. Leemann, S. Ferreiro, J. Skibsted, Experimental studies and thermodynamic modeling of the carbonation of Portland cement, metakaolin and limestone mortars, Cem. Concr. Res., 88 (2016) 60-72.
[70] L. Black, C. Breen, J. Yarwood, K. Garbev, P. Stemmermann, B. Gasharova, Structural features of C–S–H (I) and its carbonation in air—a Raman spectroscopic study. Part II: carbonated phases, J. Am. Ceram. Soc., 90 (2007) 908-917.
[71] V. Rostami, Y. Shao, A.J. Boyd, Z. He, Microstructure of cement paste subject to early carbonation curing, Cem. Concr. Res., 42 (2012) 186-193.
[72] L. Brečević, A.E. Nielsen, Solubility of amorphous calcium carbonate, J. Cryst. Growth, 98 (1989) 504-510.
[73] T. Ogino, T. Suzuki, K. Sawada, The formation and transformation mechanism of calcium carbonate in water, Geochimica et Cosmochimica Acta, 51 (1987) 2757-2767.
[74] M. Zajac, L. Irbe, F. Bullerjahn, H. Hilbig, M.B. Haha, Mechanisms of carbonation hydration hardening in Portland cements, Cem. Concr. Res., 152 (2022) 106687.
[75] M. Zajac, A. Lechevallier, P. Durdzinski, F. Bullerjahn, J. Skibsted, M. Ben Haha, CO_2 mineralisation of Portland cement: Towards understanding the mechanisms of enforced carbonation, J. CO_2 Util., 38 (2020) 398-415.

[76] W. Ashraf, J. Olek, Carbonation activated binders from pure calcium silicates: Reaction kinetics and performance controlling factors, Cem. Concr. Compos., 93 (2018) 85-98.
[77] L. Nicoleau, A. Nonat, D. Perrey, The di-and tricalcium silicate dissolutions, Cem. Concr. Res., 47 (2013) 14-30.
[78] K. Scrivener, R. Snellings, B. Lothenbach, A practical guide to microstructural analysis of cementitious materials, Crc Press Boca Raton2016.
[79] A. Korpa, T. Kowald, R. Trettin, Phase development in normal and ultra high performance cementitious systems by quantitative X-ray analysis and thermoanalytical methods, Cem. Concr. Res., 39 (2009) 69-76.
[80] J. Piasta, Heat deformations of cement paste phases and the microstructure of cement paste, Mater. Struct., 17 (1984) 415-420.
[81] H.E.D.H. Seleem, A.M. Rashad, T. Elsokary, Effect of elevated temperature on physico-mechanical properties of blended cement concrete, Constr. Build. Mater., 25 (2011) 1009-1017.
[82] F. Zunino, J. Castro, M. Lopez, Thermo-mechanical assessment of concrete microcracking damage due to early-age temperature rise, Constr. Build. Mater., 81 (2015) 140-153.
[83] Y. Fu, Y. Wong, C. Tang, C. Poon, Thermal induced stress and associated cracking in cement-based composite at elevated temperatures—Part I: Thermal cracking around single inclusion, Cem. Concr. Compos., 26 (2004) 99-111.
[84] K. Sakata, A study on moisture diffusion in drying and drying shrinkage of concrete, Cem. Concr. Res., 13 (1983) 216-224.
[85] P.K. Mehta, P.J. Monteiro, Concrete: Microstructure, Properties and Materials. , McGraw-Hill2006.
[86] A. Lau, M. Anson, Effect of high temperatures on high performance steel fibre reinforced concrete, Cem. Concr. Res., 36 (2006) 1698-1707.
[87] H.F. Taylor, Cement chemistry, Thomas Telford London1997.
[88] I.G. Richardson, The nature of CSH in hardened cements, Cem. Concr. Res., 29 (1999) 1131-1147.
[89] B. Lothenbach, A. Nonat, Calcium silicate hydrates: Solid and liquid phase composition, Cem. Concr. Res., 78 (2015) 57-70.
[90] S.-H. Kang, S.-G. Hong, J. Moon, The use of rice husk ash as reactive filler in ultra-high performance concrete, Cem. Concr. Res., (2018).
[91] B. Song, C. Shi, X. Hu, K. Ouyang, Y. Ding, G. Ke, Effect of early CO_2 curing on the chloride transport and binding behaviors of fly ash-blended Portland cement, Constr. Build. Mater., 288 (2021).
[92] C.-z. Li, X.-b. Song, L. Jiang, A time-dependent chloride diffusion model for predicting initial corrosion time of reinforced concrete with slag addition, Cem. Concr. Res., 145 (2021).
[93] Y. Li, Effect of post-fire curing and silica fume on permeability of ultra-high performance concrete, Constr. Build. Mater., 290 (2021) 123175.
[94] M. Lahoti, K.K. Wong, K.H. Tan, E.-H. Yang, Effect of alkali cation type on strength endurance of fly ash geopolymers subject to high temperature exposure, Mater. Des., 154 (2018) 8-19.
[95] C. Gallé, J. Sercombe, Permeability and pore structure evolution of silicocalcareous and hematite high-strength concretes submitted to high temperatures, Mater. Struct., 34 (2001) 619-628.
[96] H. Justnes, J. Skocek, T.A. Østnor, C.J. Engelsen, O. Skjølsvold, Microstructural changes of hydrated cement blended with fly ash upon carbonation, Cem. Concr. Res., 137 (2020) 106192.
[97] D.W. Oxtoby, Homogeneous nucleation: theory and experiment, Journal of Physics: Condensed Matter, 4 (1992) 7627.
[98] M.P. Anisimov, Nucleation: theory and experiment, Russ. Chem. Rev., 72 (2003) 591-628.
[99] H. Huang, G. Ye, D. Damidot, Effect of blast furnace slag on self-healing of microcracks in cementitious materials, Cem. Concr. Res., 60 (2014) 68-82.
[100] A.M. Neville, Properties of Concrete, Fifth Edition ed., Prentice Hall, Malaysia, 2011.
[101] D. Zhang, Z. Ghouleh, Y. Shao, Review on carbonation curing of cement-based materials, J. CO_2 Util., 21 (2017) 119-131.
[102] Z. Šauman, Carbonization of porous concrete and its main binding components, Cem. Concr. Res., 1 (1971) 645-662.

[103] J.J. Chen, J.J. Thomas, H.M. Jennings, Decalcification shrinkage of cement paste, Cem. Concr. Res., 36 (2006) 801-809.
[104] X. Pan, C. Shi, X. Hu, Z. Ou, Effects of CO_2 surface treatment on strength and permeability of one-day-aged cement mortar, Constr. Build. Mater., 154 (2017) 1087-1095.
[105] Ö. Cizer, K. Van Balen, J. Elsen, D. Van Gemert, Real-time investigation of reaction rate and mineral phase modifications of lime carbonation, Constr. Build. Mater., 35 (2012) 741-751.
[106] X. Ouyang, D. Koleva, G. Ye, K. Van Breugel, Understanding the adhesion mechanisms between CSH and fillers, Cem. Concr. Res., 100 (2017) 275-283.
[107] B. Šavija, M. Luković, Carbonation of cement paste: Understanding, challenges, and opportunities, Constr. Build. Mater., 117 (2016) 285-301.
[108] M. Castellote, C. Andrade, Modelling the carbonation of cementitious matrixes by means of the unreacted-core model, UR-CORE, Cem. Concr. Res., 38 (2008) 1374-1384.
[109] I. Galan, F.P. Glasser, D. Baza, C. Andrade, Assessment of the protective effect of carbonation on portlandite crystals, Cem. Concr. Res., 74 (2015) 68-77.